Journal of Volcanology and Geothermal Research 428 (2022) 107580

Contents lists available at ScienceDirect

Journal of Volcanology and Geothermal Research

journal homepage: www.journals.elsevier.com/journal-of-volcanology-and-geothermal-research

Stratigraphy and eruptive history of Corbetti Caldera in the Main Ethiopian Rift

David J. Colby [a,*], David M. Pyle [a], Karen Fontijn [b], Tamsin A. Mather [a], Abate A. Melaku [c], Million A. Mengesha [d], Gezahegn Yirgu [d]

[a] Department of Earth Science, University of Oxford, United Kingdom
[b] Laboratoire G-Time, Department of Geosciences, Environment, and Society, Université libre de Bruxelles, Belgium
[c] School of Earth and Environmental Sciences, University of St. Andrews, United Kingdom
[d] School of Earth Sciences, Addis Ababa University, Ethiopia

ARTICLE INFO

Keywords:
Silicic volcanism
Eruptive history
Peralkaline
Main Ethiopian Rift

ABSTRACT

The East African Rift (EAR) hosts the highest density of peralkaline volcanoes of any region globally, making it an ideal location to study the subaerial and magmatic processes of peralkaline volcanism. Corbetti Caldera is one such peralkaline centre found within the southern part of the Main Ethiopian Rift (MER), a segment of the EAR. Corbetti is actively deforming and has previously undergone large-scale Plinian eruptions. However, our broader understanding of Corbetti's evolution is limited. Here we present a detailed study of the pre-, syn-and post-caldera eruptive deposits and compile them into a composite stratigraphy of the volcanic sequence. We find evidence for multiple previously undocumented large-scale eruptions, including the deposition of two pre-caldera lithic lag breccias, and we identify three additional post-caldera obsidian lavas. We constrain the age of a young Tuff Cone, Biftu, which sits outside the caldera walls, to <7375 ± 54 cal BP through ^{14}C dating of shells within an associated PDC deposit. The Wendo Koshe Cone, the most recent cone within the complex, is interpreted as the remains of two cones that opened in close proximity to each other and formed the vents for two pyroclastic eruptions: Bedded Pumice and Wendo Koshe Younger Pumice (WKYP). There is abundant evidence for the occurrence of pyroclastic density currents (PDC) within the caldera, usually associated with pumice cone-forming eruptions. These flow deposits rarely extend beyond the caldera walls. From our compiled stratigraphy, we estimate a recurrence rate of one eruption per 300–400 years over the last 2.3 ky.

These findings are especially significant as Corbetti is earmarked for potential geothermal exploration, and an understanding of eruptive frequency and style provides vital context to assess the potential hazards associated with this future infrastructure.

1. Introduction

Quaternary volcanism within the Main Ethiopian Rift (MER) has been characterised by a diverse range of volcanic activity (Fontijn et al., 2018), from large scale caldera-forming eruptions (Hutchison et al., 2016a, 2016b; Rampey et al., 2010; Tadesse et al., 2022) to pumice cone eruptions (Clarke et al., 2019, 2020) and the eruption of basaltic scoria cones (Hunt et al., 2019; Mazzarini et al., 2004). There have been no confirmed eruptions within the MER since the 19th century, therefore, our understanding of the past dynamics of volcanism and potential future activity can only be gained through investigations of the geological record. The products of peralkaline volcanism dominate within the rift (Clarke et al., 2019); however, this type of eruption has not been observed directly, making the MER a vital place to study the properties of peralkaline magmas and their deposits (Gleeson et al., 2017; Iddon et al., 2019; Iddon and Edmonds, 2020; Macdonald and Gibson, 1969; Rooney et al., 2012; Tadesse et al., 2019 and references therein). Many of the large silicic calderas of the rift lie close to large population centres and densely populated rural communities. Over 10 million people live within 30 km of one of Ethiopia's 59 Holocene volcanoes, and Ethiopia is ranked as having the 5th highest risk to human life from volcanic hazards of any country in the world (Aspinall et al., 2011; Loughlin et al., 2015; Vye-Brown et al., 2015).

Ethiopia is increasingly looking to exploit the geothermal potential

* Corresponding author.
E-mail address: david.colby@pmb.ox.ac.uk (D.J. Colby).

https://doi.org/10.1016/j.jvolgeores.2022.107580
Received 6 December 2021; Received in revised form 9 May 2022; Accepted 16 May 2022
Available online 21 May 2022

of several of the large silicic centres within the rift. Aluto has hosted a geothermal plant since 1998, and plans are in place to develop sites at Tullu Moye and Corbetti (Altaye, 1984; Biggs et al., 2011; Gíslason et al., 2015; Hutchison et al., 2015). These projects could be hugely beneficial to Ethiopia's economic and energy security; however, we know little about the volcanic history or the volcanic hazards for many of the planned sites.

1.1. Regional setting

The MER forms one segment of the East African Rift (EAR), a 4000 long km zone of extensional deformation caused by the divergence of the Arabian and Somalian plates from the Nubian Plate (Ebinger, 2005). The MER developed asynchronously across three main sectors: the northern (< 30 Ma), southern (18 Ma), and Central rift (6–11 Ma) (Boone et al., 2019; Purcell, 2018; WoldeGariel et al., 1992) and is the classic example of an oblique continental rift, connecting the Afar Depression to the north, and the Turkana depression and Kenyan Rift to the south (Fig. 1; [Ebinger, 2005]). At ~2 Ma the development of the Wonji Fault Belt (WFB), a region within the N-MER (and incipient in the C-MER) containing numerous short, right-stepping echelon faults, resulted in the migration of strain away from the boundary faults and towards the centre of the rift (Casey et al., 2006; Corti, 2009; Corti et al., 2022; Ebinger and Casey, 2001; Kurz et al., 2007; Mohr et al., 1980; Pizzi et al., 2006). This fault belt, and the subsequent development of magmatic segments, marked a transition towards magma-dominated deformation/rifting (Kendall et al., 2005). This transition to magma-assisted deformation and rifting is key for enabling the style and distribution of volcanism seen across the rift today. The cross rift faults within the WFB and those linked to early stages of rift development play a critical role in determining the location, shape, and orientation of calderas, as well as controlling the position of post-caldera vents (Corti et al., 2022; Maestrelli et al., 2022; Mohr et al., 1980; Robertson et al., 2016).

1.2. Corbetti Caldera

Corbetti is located within the southernmost part of the rift (Fig. 1) and is one of the largest calderas within the MER. It has followed an evolutionary pattern similar to other caldera volcanoes within the MER, beginning with a shield-building phase of peralkaline rhyolite lava flows, followed by at least one caldera-forming eruption, the inferred deposits of which are dated to ca. 182 ± 28 ka (Hutchison et al., 2016a). Subsequent volcanism focused around three post-caldera edifices (Artu, Urji, and Chabbi) and a rhyolitic cone (Biftu Tuff Cone), situated outside the south-eastern caldera wall (Fig. 2; [Clarke, 2020; Fontijn et al., 2018; Hunt et al., 2019; Rapprich et al., 2016]). The caldera rim has an irregular elliptical shape, approximately 15.6 × 10.9 km along the long and short axis respectively (Hunt et al., 2019), with steep cliffs on the northern and southern rim and broader, heavily incised slopes on the western side. The eroded remains of Artu cone partly cover the north-eastern section of the caldera, and younger products from Chabbi shield entirely cover the eastern portion of the caldera wall.

Previous studies have highlighted the variety of deposits associated with the post-caldera edifices. Both Urji and Chabbi have experienced explosive and effusive eruptions from numerous vents (Di Paola, 1971; Fontijn et al., 2018; Hunt et al., 2019; Rapprich et al., 2016) however, the youngest eruptions from Urji were predominantly explosive (Fontijn et al., 2018; Rapprich et al., 2016) whilst the eruption of obsidian lava

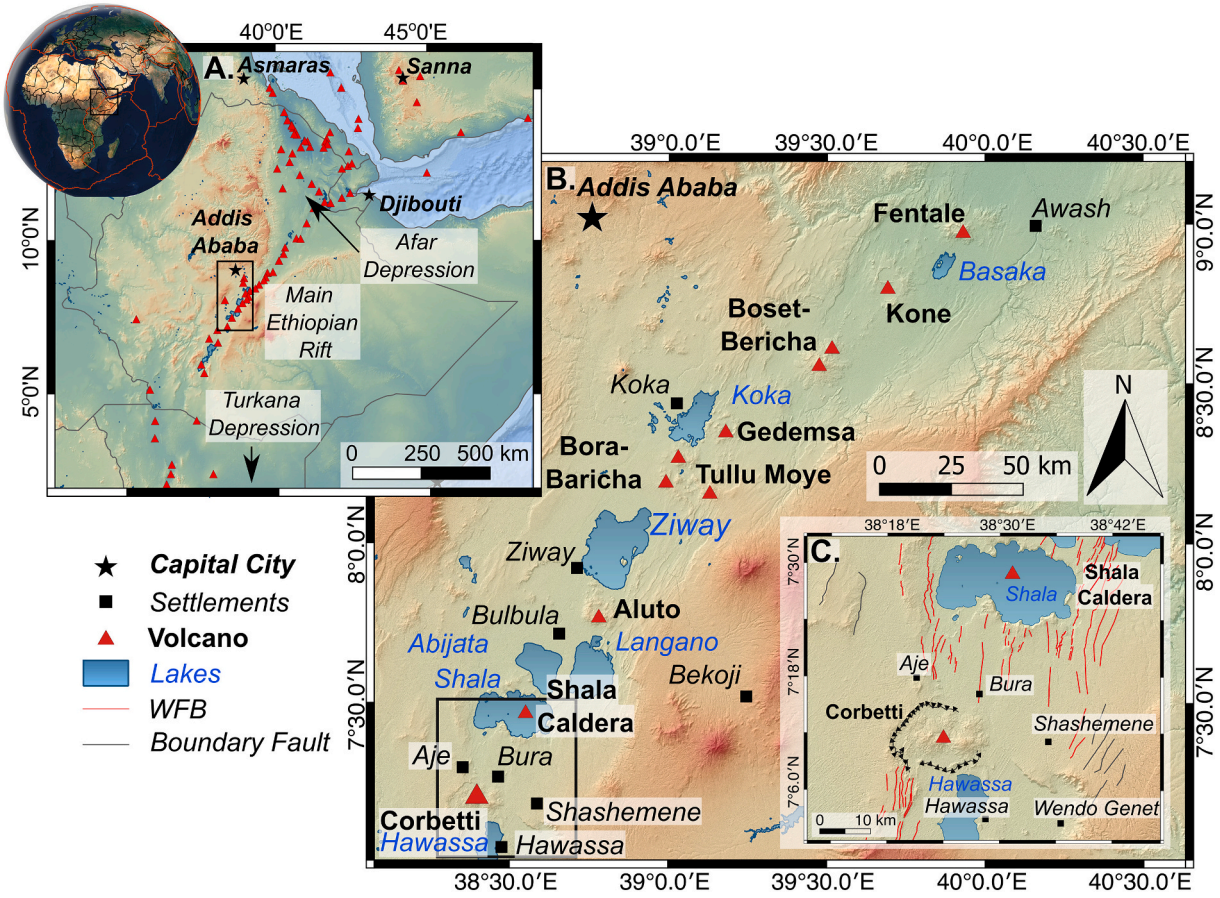

Fig. 1. A) Overview map of the East African Rift (EAR) showing major fault structures and location of silicic volcanoes. B) Overview map of the Main Ethiopian Rift (MER) showing the location of central silicic volcanoes and major settlements. Corbetti, the focus of this study, is in the southern part of the MER. C) Map showing location of Corbetti Caldera and a section of the Wonji Fault Belt (WFB). Faults after (Agostini et al., 2011).

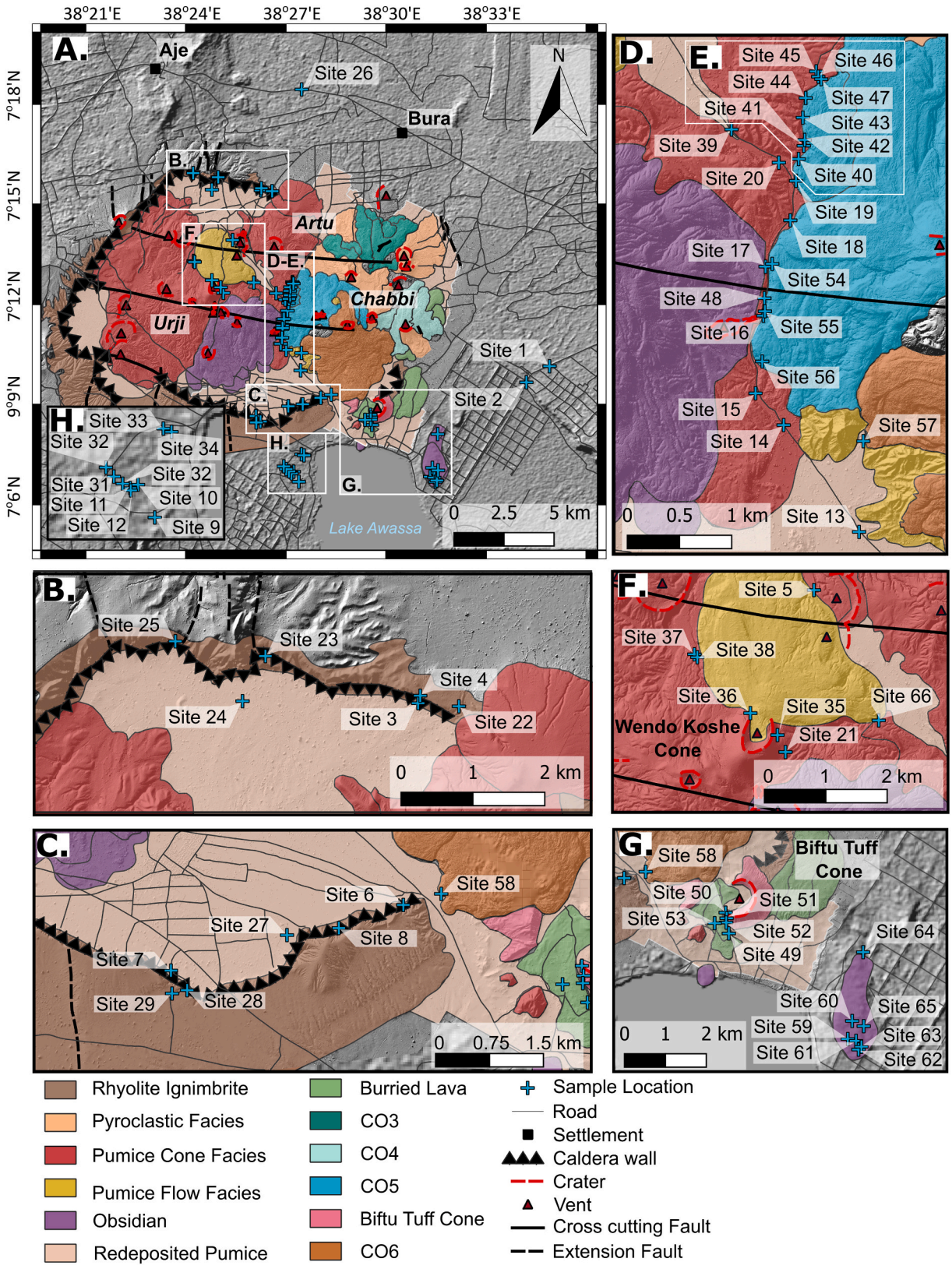

Fig. 2. A) Geological setting of Corbetti Caldera, highlighting the major features, geological facies within the caldera and the sampling locations for this study [after Rapprich et al., 2016, Hunt et al., 2019, Clarke, 2020] B) Detail of sample locations in the Northern Caldera wall. C) Detail of sample locations in Southern caldera wall. D)Detail of Central Caldera sample locations E) Detail of Central Gully section sample locations. F) Detail of sample locations around the slopes of Urji. G) Detail of sample locations around the Biftu Tuff Cone and older pre-caldera deposits. H) Detail of sample locations of drainage gullies.

flows occurred most frequently on Chabbi (Di Paola, 1971; Fontijn et al., 2018; Macdonald and Gibson, 1969; Rapprich et al., 2016). Across both edifices the erupted products are typically geochemically homogenous, crystal-poor peralkaline rhyolites (Fontijn et al., 2018; Rapprich et al., 2016).

Previous studies have identified two major explosive eruptions, the Bedded Pumice eruption and Wendo Koshe Younger Pumice (WKYP) (Fontijn et al., 2018; Rapprich et al., 2016). Deposits of these two eruptions have been correlated across multiple intra-caldera localities and at locations outside the caldera walls (Fontijn et al., 2018), including lake sediment cores (Martin-Jones et al., 2017). The Bedded Pumice unit is a rhythmically bedded pumice fall deposit containing thin cm-thick ash-rich flow packages and obsidian lithics. It is attributed to the products of a pulsating eruption that gradually built a conical deposit and is best preserved and exposed within the caldera (Fontijn et al., 2018). The Bedded Pumice is inferred to have had an approximate eruption magnitude of 4 (Fontijn et al., 2018) and is capped by a paleosol that stains the upper 30 cm of the unit. At distal locations, the Bedded Pumice unit is overlain by the geochemically-similar deposits of the WKYP eruption, a massive pumice fall deposit that lacks obsidian clasts (Fontijn et al., 2018; Rapprich et al., 2016). Mapping the spatial distribution of this unit yielded an estimated minimum deposit volume of 1.3 km^3 and an approximate magnitude of 5 (Fontijn et al., 2018; Rapprich et al., 2016). Based on this mapping and observed field deposits, the source of this eruption is inferred to be the Wendo Koshe Cone (Fig. 2F), the most recent cone on the flanks of Urji. Soil-carbon from the paleosol beneath WKYP is radiocarbon dated to $<2301 \pm 120$ cal BP (Rapprich et al., 2016). Based on the observations of volcanic deposits from Corbetti, Fontijn et al. (2018) and Martin-Jones et al. (2017) estimated the recurrence interval of explosive eruptions to be around one eruption per 700–1000 years. However, as noted by McNamara et al. (2018), this is likely an underestimate.

Remote-sensing studies demonstrate the presence of an active geothermal system at Corbetti and provide evidence for a shallow magma plumbing system influenced by pre-existing E-W trending faults (Gíslason et al., 2015; Lavayssière et al., 2019; Lloyd et al., 2018b). Complementary InSAR studies show Corbetti has been actively deforming since at least 2009, uplifting at 6.6 ± 1.2 cm yr^{-1} (Biggs et al., 2011; Gottsmann et al., 2020; Lloyd et al., 2018a, 2018b). This is attributed to the intrusion of $\sim 10^{11}$ kg yr^{-1} mafic magma at ~ 7 km depth (Gottsmann et al., 2020). This demonstrates that Corbetti still has an active magma system and, therefore, still has eruptive potential. Despite this, considerable uncertainty surrounds the details of the eruptive history of Corbetti, its pre-caldera activity, and the controls on eruptive style.

The purpose of this study is to present a revised interpretation of the pre-and post-caldera eruptive activity of Corbetti, based on a new investigation of the eruptive deposits and their processes of emplacement and to document their compositions (whole rock and glass, major and trace element analysis), building on the work of previous studies (Fontijn et al., 2018; Martin-Jones et al., 2017; Rapprich et al., 2016). These data are compiled into a composite stratigraphy identifying discrete phases of activity and presented as a relative chronology for activity at Corbetti.

2. Samples and methods

2.1. Field campaign

A 3.5-week field campaign was undertaken in January 2020, focusing on five main regions within the caldera (Fig. 2). These regions are a portion of the northern caldera wall (Fig. 2B), the southern caldera wall (Fig. 2C), road cuts through the central caldera (Fig. 2D), exposures in a central gully (Fig. 2E), and exposures on the slopes of Urji (Fig. 2F). These regions were selected as they were relatively accessible and encompassed the main periods of pre-and post-caldera activity, enabling the lateral tracing of units across multiple localities. This allowed for the establishment of correlations within the field. Several locations, such as portions of the western caldera and flanks of Chabbi, could not be visited due to challenges surrounding access and time constraints. However, investigation at several locations outside of the caldera (around the Biftu Tuff Cone (Fig. 2G) and in drainage gullies near Lake Hawassa [Fig. 2H]) were studied and yielded information on the explosive eruptions at Corbetti and the eruption of the extra-caldera, Biftu Tuff Cone (Fig. 2G).

At each location units were systematically logged and sampled to capture any changes in texture and compositions. Fig. 2 highlights the sample locations, and field photos show the stratigraphic location of the collected samples.

2.2. Stratigraphic framework

Previous studies of Corbetti have highlighted the challenge of clearly distinguishing between eruptive units due to laterally discontinuous, highly variable lithofacies and geochemical similarities (Fontijn et al., 2018). Here we present stratigraphies from multiple sections of the caldera, highlighting correlations based upon the lateral continuity of marker horizons (e.g., paleosols, fall deposits, etc.), and outcrops of similar lithofacies, before compiling them into a wider composite stratigraphy. Not all units within a given region could be correlated accurately due to high spatial variability and low confidence in their stratigraphic position. These units are excluded from the composite stratigraphy; however, we highlight them in the relevant sections. Once compiled, the complete composite stratigraphy was separated into pre-, syn-, and post-caldera phases of activity and incorporated with a relative chronology established for Chabbi and the Biftu Tuff Cone (Clarke, 2020; Hunt et al., 2019; Rapprich et al., 2016). Units are referred to in terms of their lithofacies to highlight distinguishing features using the approach of Branney and Kokelaar (2002) (for abbreviations and definitions, see Table 1).

2.3. Geochemistry and ^{14}C dating

Tephra and lava samples were selected to provide broad coverage of pre-and post-caldera activity at Corbetti and aimed to complement existing sample sets (Fontijn et al., 2018; Rapprich et al., 2016). Samples were cleaned, oven-dried, crushed, and powdered in an agate ball mill before being sent to Activation Labs (Ontario, Canada) in two batches

Table 1
Definitions of lithofacies notations used in this study (Branney and Kokelaar, 2002).

Notation	Definition	Description
mT	Massive tuff	An ash-rich tuff where the structure is massive
mL	Massive lapilli	A unit dominated by lapilli size (2–64 mm) clasts with a massive structure
mLT	Massive lapilli tuff	A tuff with lapilli sized clasts and a massive structure
dsT	Diffusely stratified tuff	An ash-rich tuff with poorly defined stratification
dsLT	Diffusely stratified lapilli tuff	A tuff with poorly defined stratification containing lapilli sized clasts. Clasts occasionally follow stratification
sT	Stratified tuff	An ash-rich tuff which shows clear stratification caused by slight changes in grain size and/or colour of ash
maccT	Massive ash aggregate bearing tuff	A massive ash-rich tuff containing ash aggregates
xsLT	Cross stratified lapilli tuff	A lapilli-bearing tuff which displays a cross-stratified fabric. These may be cross beds (> 10 mm) or cross laminations (< 10 mm)
dslBr	Diffusely stratified lithic rich breccia	Clast supported, lithic-rich unit containing compositional diverse blocks >64 mm. Shows poorly defined stratification

for major and trace element analysis. Samples were fused into beads and digested in a 5% nitric acid solution until dissolved (around 45 minutes). Major elements were determined through ICP-OES and trace elements through ICP-MS. Detection limits are better than 0.01% for major elements and better than 30 ppm for trace elements.

Several outcrops in drainage gullies close to the shore of Lake Hawassa (Fig. 2H) contained abundant reworked shells of multiple gastropod species. Two shells of *Melanoides tuberculata* from two horizons underwent ^{14}C dating at Beta Analytic to provide a maximum age for the deposits. Samples were pre-treated using an acid etch. They were washed in deionised water to remove debris and then crushed and repeatedly subjected to HCl etches to eliminate secondary carbonate components. Samples were analysed by accelerator mass spectrometry (AMS), and the data were corrected for isotopic fractionation and calibrated using INTCAL20 (Reimer et al., 2020). Samples were also analysed for $\delta^{18}O$. $\delta^{13}C$ was measured on pre-treated samples acidified in a gas bench to produce CO_2 and then analysed in an isotope ratio mass spectrometer.

3. Results: stratigraphy

3.1. Northern caldera wall (NCW)

The northern caldera wall (NCW; See Fig. 2B for sample locations) records some of the oldest activity at Corbetti, however, exposures are limited due to heavy erosion, burial by younger deposits and inaccessible outcrops. At the base of the North Caldera wall, a > 15 m thick rhyolite lava (NCW_A; Fig. 3A, Fig. 4A, Table 2) is overlain at Sites 24 and 25 (Fig. 2B) by a large bedded tephra succession (NCW_B; Fig. 3A) dipping 17° to the east. The sequence at Site 24 is covered by a 3.8 m thick rhyolite lava (NCW_C) and capped by a second sequence of bedded tephra horizons (NCW_D; Fig. 3B). To the east, at Sites 3 and 4 (Fig. 2B), this lava and tephra succession is absent. Instead, a poorly consolidated red ignimbrite (NCW_E; Fig. 3C) outcrops at the base of the sequence (this unit is also observed outside the caldera walls at Site 2 [Fig. 2A]). This red ignimbrite is overlain by a eutaxitic welded ignimbrite (NCW_F; Fig. 3C & D) and a poorly consolidated reworked pumice horizon (NCW_G; Fig. 3C). Slightly north of this exposure, moving up the caldera wall to Site 4, a sequence of ash aggregate bearing tuff horizons is observed (NCW_H; Fig. 3E). A similar sequence of sintered and loosely consolidated ash horizons is also seen at Site 23 (Fig. 2B, Fig. 3F and Supplementary Information (SI) A1). Based upon the similarities in lithofacies and stratigraphic positions, units at Site 4 and Site 23 are correlated as the same unit (NCW_H).

In our compiled stratigraphy for this section (Fig. 4A) of the caldera, we propose that units NCW_A - NCW_D were deposited before the caldera-forming eruption. The abrupt change in lithofacies between Sites 24 and 23 makes it difficult to draw clear correlations between these two sections of the caldera wall. A fault, seen as a marked drop in the height of the caldera wall, divides these two sections (Fig. 2B; [Hunt et al., 2019]). This may explain the abrupt change in lithofacies observed between these locations.

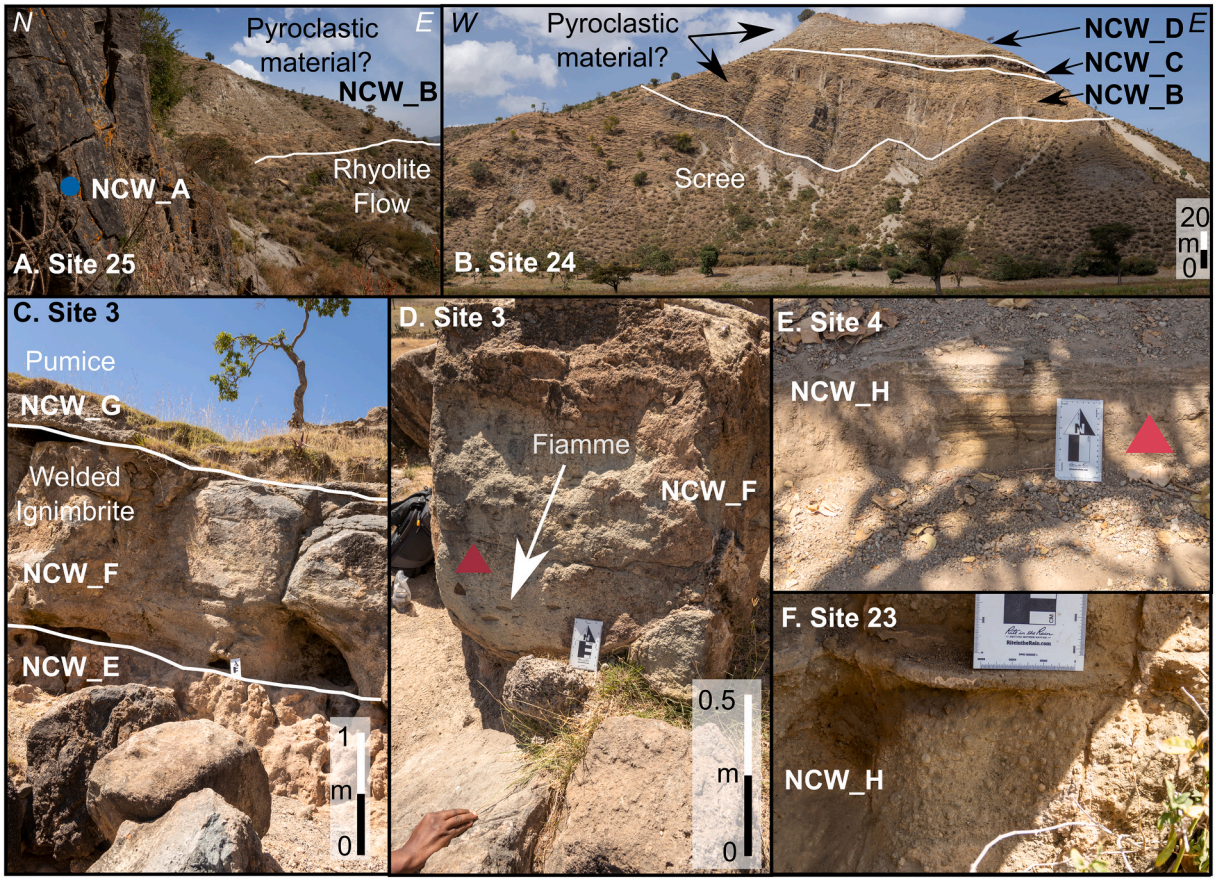

Fig. 3. Field photos highlight outcrops in the Northern Caldera wall. Symbols denote location of collected samples and site localities are marked in Fig. 2. A) Site 25 showing a jointed rhyolite lava (NCW_A) and the contact between an overlying pyroclastic succession, inferred to be NCW_D. B) Site 24 showing the pyroclastic succession (NCW_B) capped with a thin lava (NCW_C) and further pyroclastic succession (NCW_D). C) Welded ignimbrite at Site 3, showing the contact between the underlying red ignimbrite. D) Detail of the welded ignimbrite (NCW_F). E) Laminated ash-rich horizons (NCW_H) at Site 4. Horizons vary between loose unconsolidated ash and sintered ash. F) Ash aggregate (Accretionary Lapilli) bearing horizon at Site 23 (NCW_H). (For interpretation of the references to colour in this figure legend, the reader is referred to the web version of this article.)

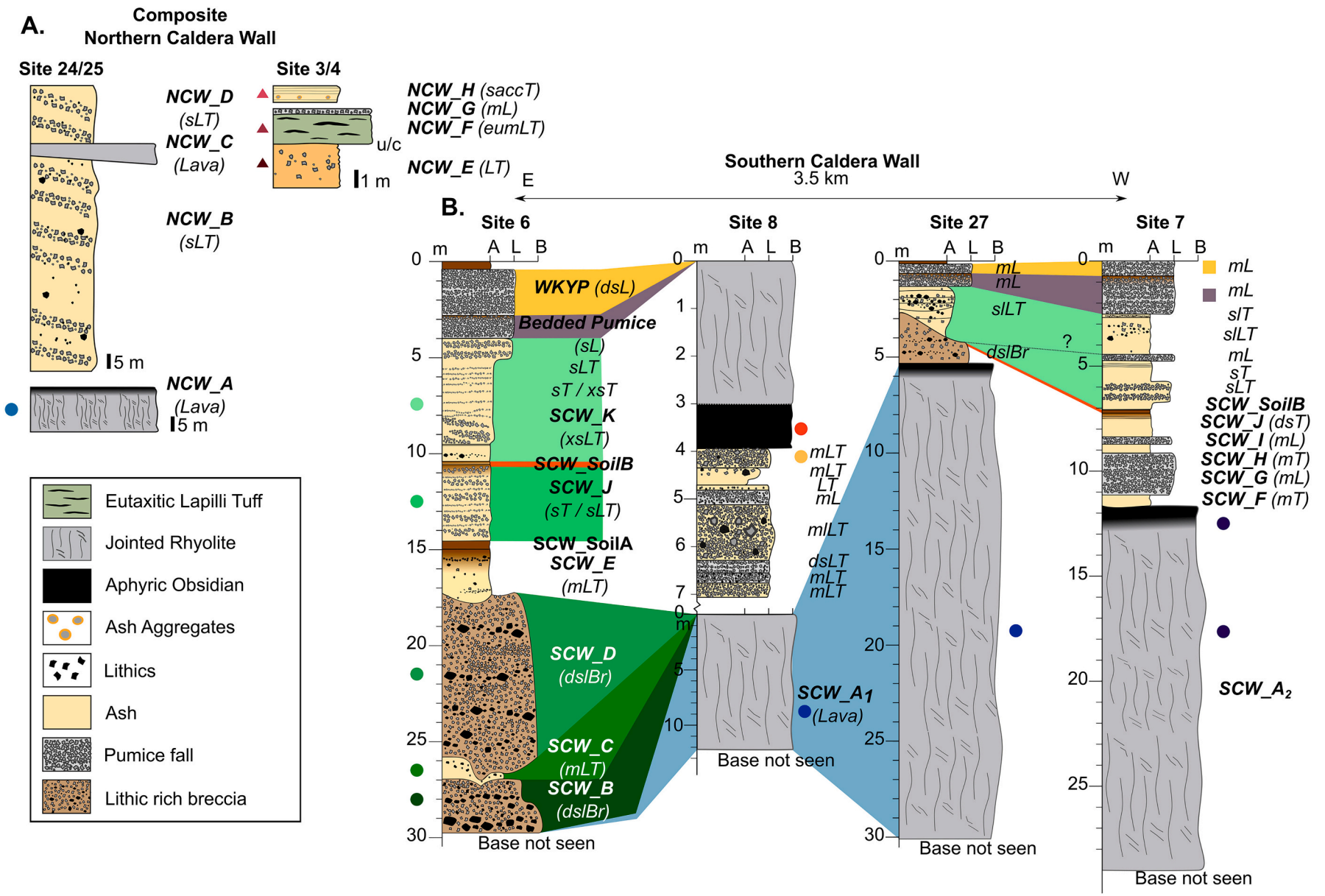

Fig. 4. A) Stratigraphic log of units exposed in the northern caldera wall (Fig. 2B) and described in Table 2. B) Stratigraphic logs of exposures in the Southern Caldera wall (Fig. 2C) highlighting lateral correlations between outcrops. Units described in Table 3. Symbols denote the location of samples which underwent geochemical analysis (See section 4).

Table 2
Descriptions and interpretations of units exposed in sections of the northern caldera walls (Figs. 2B for sample locations, Figs. 3 for field photos & Fig. 4A for stratigraphic log). Units presented from youngest to oldest. Table 1 outlines the description of lithofacies.

Unit	Type locality	LF	Thickness (m)	Description	Interpretation
NCW_H *(Top of succession)*	Site 4/ Site 23	maccT	0.3	A stratified ash-rich unit containing sparse 5–10 mm ash aggregates, most likely accretionary lapilli. Ashy horizons varied between cemented and poorly consolidated and are 50–100 mm thick (Fig. 3E-G).	Multiple dilute, ash-rich PDC deposits. Ash aggregates (likely accretionary lapilli) may suggest some interaction with water during the eruption (Brown et al., 2010, 2012), potentially phreatomagmatic. Stratification suggests pulsating nature of eruption with numerous waves of PDCs being generated.
NCW_G	Site 3	mL	0.37	Poorly sorted pumice deposit comprised of clast-supported, angular pumice ranging in size between 5 and 50 mm (Fig. 3C).	Locally eroded pumice deposit that is incorporated with paleosol
NCW_F	Site 3	eumLT	1.7	Green, massive, eutaxitic lapilli-tuff with fiamme ~50 mm long. Sparse lithics. Unconformably overlies NCW_E (Fig. 3C&D)	Welded ignimbrite may be related to underlying ignimbrite.
NCW_E	Site 3	mLT	2.5	Reddish, ash-rich, matrix-supported deposit with sparse pumice clasts and lithics (5–20 mm). Unit is poorly consolidated (Fig. 3C).	Dilute PDC deposit likely associated with the 182 ± 28 ka ignimbrite identified by (Hutchison et al., 2016a; Vidal et al., 2022)
NCW_D	Site 24	s/mLT	15.4	A succession of matrix-supported ash-rich horizons. Evidence of sparse pumice and lithics (Fig. 3B)	Dilute PDC deposits. Multiple horizons indicate the passage of several flows, may indicate sustained eruption.
NCW_C	Site 24	Lava	3.8	Blocky lava deposit, some jointing observed (Fig. 3B).	Small lava deposit, lack of access prevented further investigation.
NCW_B	Site 24	s/mLT	~70	Large pyroclastic succession containing multiple horizons of matrix-supported, ash-rich horizons. Horizon's dipping ~17° E. Some m scale stratification was observed (Fig. 3B).	Deposition of multiple PDCs. Variation in bedding structures indicates varying conditions at the vent and in the flow during deposition.
NCW_A *(Base of succession)*	Site 25	Lava	> 15 (base not seen)	Jointed rhyolitic lava with some localised flow banding (Fig. 3A).	Deposit of rhyolite lava emplaced during Corbetti's shield building phase. Jointing indicates slow cooling

Hutchison et al., (2016a) describe the ignimbrite associated with the caldera-forming eruption as a red, welded ignimbrite containing obsidian fiamme. Whilst NCW_E is not welded, we infer it to be an unwelded facies of the deposit. However, a detailed description of the dated ignimbrite is unavailable, and a lack of location and stratigraphic information makes this correlation tentative. The unconformity between NCW_E and F indicates the green welded ignimbrite is from a separate eruption. It is inferred that the emplacement of NCW_E - G occurred after the deposition of NCW_A - D due to the absence of units observed in the western portion of the caldera wall outcropping above the green welded ignimbrite. We proposed the ignimbrite was deposited in a paleovalley thus explaining its absence at the top of the succession at Site 25 (Fig. 2B).

3.2. Southern caldera wall (SCW)

Four localities in the southern portion of the caldera wall, which encompass the pre-and post-caldera activity, were studied in detail (Sites 6, 7, 8 and 27; Fig. 2C), and observations of the stratigraphy are presented in Table 3 and Fig. 4B. The base of the Southern Caldera wall is comprised of thick (>10 m) lavas (Fig. 5 & SI A2), similar to those observed in the Northern Caldera Wall. Two distinct lava units have been identified by lateral tracing of the units in the field, the distance between the two outcrops and a lack of exposures between the two localities. SCW_A_1 outcrops at Site 8 and 27 (SI A2), and SCW_A_2 outcrops at Site 7 (Fig. 5). The relative ages of these two deposits could not be constrained due to an absence of clear contact between them.

Correlating units overlying these two rhyolitic lavas (SCW_A_1 & SCW_A_2) is challenging due to a wide variation in lithofacies and spatial variability of outcropping units. At Site 6, lava deposits (SCW_A_1) are absent and the base of the exposure is comprised of two large lithic-rich breccias (SCW_B & SCW_D) inter-bedded with massive, ash-rich horizons (SCW_C & SCW_E). This sequence is capped by a paleosol (SCW_SoilA; Figs. 4 & 6). Units SCW_B-E are not observed at other localities and are inferred to be deposited in a paleovalley created, in part, by the deposition of SCW_A_1, which is seen to dip away to the east. A lithic breccia is also seen above SCW_A_1 at Site 27 (SI A2), however it is unclear if this is the same unit as the lithic breccias outcropping at Site 6.

Further to the west at Site 7, a succession of pumice-fall and ash-fall deposits (SCW_F - I; Table 3; SI A2) is observed overlying the jointed lava (SCW_A_2). These units are only observed at this location and therefore the relative timing of their eruption is difficult to establish. The sequence is capped by a diffusely stratified tuff stained by an overlying paleosol. The paleosol (Fig. 4B, 5) is tentatively correlated to SCW_SoilB and the underlying tuff with SCW_J, based upon the overlying succession sharing similarities to the lithofacies observed at Site 6 (Fig. 6).

The upper portion of the South Caldera Wall is dominated by a large ash-rich succession which at Site 6 comprises multiple units of ash-rich, matrix-supported tuffs containing sparse lithics and lenses of pumice (SWC_J & K Fig. 6C) separated by a paleosol (SCW_SoilB). Two pumice horizons cap the succession and are seen to outcrop at several locations across the SCW (Fig. 6C). The lower pumice horizon shows diffuse to massive bedding and sparse obsidian lithics are observed at the Site 7 outcrops (Fig. 5C, D). The upper 0.3 m of the horizon are reverse graded and stained by an overlying paleosol. This unit shares features with and is correlated to the Bedded Pumice unit identified by Fontijn et al. (2018). The upper pumice horizon is massive and obsidian lithics are absent. This has been correlated to the WKYP deposits, as described in Fontijn et al. (2018) and Rapprich et al. (2016). These units are significant as they are the most widely dispersed and easily recognisable within the caldera making them an important stratigraphic marker horizon. The deposits of the Bedded Pumice unit and WKYP are seen in the upper parts of the succession at Site 7, as is the underlying matrix-supported PDC deposit (SCW_K; Fig. 5C). This ash-rich PDC deposit is also seen in the upper section of the outcrop at Site 27 (Fig. 2C and SI A2). Here the unit is matrix-supported and stratified and contains

Table 3
Description and interpretation of units exposed in the Southern caldera wall (Fig. 2C). Stratigraphic log outlined in Fig. 4B. Field photos of outcrops are found in Figs. 5 & 6.

Unit	Type locality	LF	Thickness (m)	Description	Interpretation
SCW_SoilC	–	Soil	0.43	Organic layer with reworked pumice (Fig. 5).	Topsoil
WKYP	Site 6	dsL	2.43	Massive to diffusely stratified, clast supported pumice deposit. Pumice ranges in size between 10 and 50 mm. Well sorted with sparse larger clasts (Figs. 5, 6).	Distal pumice fall deposit of the WKYP deposit identified in Fontijn et al. (2018) and Rapprich et al. (2016). Slight bedding suggests minor changes in conditions at the eruptive vent.
Bedded Pumice	Site 6	dsL	1.18	Diffusely stratified, ~ 10–200 mm, lapilli horizon. Clast supported, angular pumice ranges in size between 5 and 30 mm. Top ~0.4 m are stained by an overlying paleosol. However, paleosol is not visible as a distinct horizon (Figs. 5, 6).	Distal pumice fall deposit of the Bedded Pumice of Fontijn et al. (2018). Bedding patterns suggest varying conditions at the eruptive vent.
SCW_K	Site 6	xsLT/ sT	6.51	Cross-stratified to stratified ash-rich tuff with lenses of pumice on the lee side of dune structures. Pumice ranges in size from 10 to 60 mm (Fig. 6).	Dilute, ash-rich PDC, likely phreatomagmatic in origin, with lenses of coarse pumice. Sedimentary structures indicate changes in conditions at the lower flow boundary (LFB) (Branney and Kokelaar, 2002) and varying depositional regimes through space and time. The thickness of the deposit indicates a significant, sustained event
SCW_SoilB	Site 6	Soil	0.1	Dark organic layer (Fig. 6)	Paleosol
SCW_J	Site 6	sT/sLT	4.25	Deposit varies between stratified tuff and stratified lapilli tuff. Lenses of coarse-grained pumice (~30–60 mm) and finer-grained pumice (~5–10 mm) occur throughout the deposit (Fig. 6).	Records passage of a PDC that transitioned between dilute and granular flow, possibly phreatomagmatic. Varying conditions at the lower flow boundary resulted in the deposition of coarser and finer-grained material at different intervals.
SCW_I	Site 7	mL	0.37	Similar to SCW_G. Massive lapilli horizons are comprised of well-sorted angular pumice which do not exhibit any bedding features nor contains lithics. Pumice ranges in size from 5 to 10 mm (Fig. 6).	Pumice fall deposit
SCW_H	Site 7	mT	0.44	Similar to SCW_F. Massive tuff horizon comprising fine-grained ash appears to be lithic-free. No clear signs of changes in grain size; bedding features are absent (Fig. 5).	Ash-fall deposit
SCW_G	Site 7	mL	2.07	Massive lapilli horizon comprised of well-sorted angular pumice. Pumice ranges in size from 5 to 40 mm; no lithic fragments were observed (Fig. 5)	Pumice fall deposit
SCW_F	Site 7	mT	0.54	Massive tuff horizon comprised of fine-grained well-sorted ash. Unit inaccessible but appears to be lithic-free. No clear signs of changes in grain size or presence of pumice lapilli. Bedding features are absent. Unit is laterally extensive across exposure and does not display any erosive contacts (Fig. 5)	Ash-fall deposit
SCW_SoilA	Site 6	Soil	0.43	Dark organic rich layer (Fig. 6)	Paleosol
SCW_E	Site 6	mLT	2.4	Fine-grained ash horizon containing sparse lithic clasts. Contact with underlying breccia varies between gradational and erosional. Some lenses of pumice and lithics present. Pumice clasts range between 10 and 30 mm and lithics between 10 and 40 mm. A paleosol horizon has developed above this layer (Fig. 6)	Records deposition of a dilute ash-rich PDC. The gradational to erosional boundary between the underlying deposit could suggest this unit records the wanning phase of the PDC. The massive nature of the deposit indicates a fluid escape regime at the LFB (Branney and Kokelaar, 2002) with the deposition of coarser-grained lenses indicative of a spatially and temporally limited transition to a traction dominated flow regime (Branney and Kokelaar, 2002). The presence of soil indicates a sustained period of quiescence after this eruptive event.
SCW_D	Site 6	dslBr	8.66	Diffusively stratified, clast supported, lithic-rich breccia which displays a moderate degree of sorting and containing angular to sub rounded lithic clasts. Comprise of fragments of red ignimbrite, flow-banded rhyolites, and sparse obsidian fragments. Some meter-sized blocks are present in the deposits. The upper portion of the unit grades up into matrix-supported fine ash (Fig. 6).	Lithic lag breccia recording the deposition of a large granular PDC. The high concentration of lithics and remobilised ignimbrite suggest considerable remobilisation of previously erupted material. The eruption could be linked with a phase of pre-caldera edifice collapse as is observed at other MER volcanoes (Tadesse et al., 2022) and large scale caldera systems (Druitt, 1985). The large scale of this deposit suggests a sustained event.
SCW_C	Site 6	mlT	1.2	Unconsolidated ash with lenses of angular 20–100 mm lithics. Unit pinches and swells. Pumice is present in thicker sections and the concentration of pumice increases towards the top of the horizon. Unconformably overlies SCW_C (Fig. 6).	Pinch and swell structures suggest deposition via a current with a spatially variable depositional regime. Ash rich, massive nature suggests a dilute PDC dominated by tractional forces. The presence of angular lithics suggests limited transport time in the current reducing the degree of clast interaction.
SCW_B	Site 6	dslBr	~2.86 (base not seen)	Diffusively stratified lithic-rich breccia displaying poor to moderate sorting. Unit predominantly clast-supported but grades to matrix-supported at the top of the unit, the upper ~0.3 m of which is cemented. The unit contains a diverse population of lithic clasts that making up >50% of the deposit. Lithics are primarily obsidian chips, banded rhyolite, and fragments of a red ignimbrite. Lithics are angular to sub-rounded. Lenses of coarser-grained lithic material are also seen. Pumice lapilli are present throughout, although it increases in abundance towards the top of the unit. Clasts range in size from 10 to 400 mm. A portion of the deposit displays diffuse stratification whilst the central part of the exposure displays signs of reworking (Fig. 6).	Records depositional regime of a granular PDC. The presence of ignimbrite fragments suggests remobilisation and reworking of previously deposited material indicating the eruption from which the ignimbrite fragments are sourced must have occurred before the deposition of this unit. The lithic-rich nature of the deposit could suggest a large-scale eruption. The depositing current was likely a granular flow which was strongly controlled by paleotopography created in part by the emplacement of SCW_A_1. The event could be linked to a phase of edifice collapse. A portion of the deposit shows signs of reworking
SCW_A	Site 27	Lava	~25	Jointed rhyolite lava outcrops at multiple localities in the Southern Caldera Wall. The top of the flow transitions towards glassy obsidian in places (SI A2). SCW_A_1 dips away to the east, under outcrop at Site 6 creating a paleo valley.	Pre-caldera lavas associated with the shield-building phase of Corbetti's evolution. Two flows have been identified in the southern caldera wall. SCW_A_1 at Site 8 and 27 and SCW_A_2 at Site 7.

abundant lithic clasts.

.

Units that outcrop at Site 8 have different lithofacies to other observed units in the Southern Caldera Wall (Fig. 2C & SI A3). The exposure occurs above SCW_A_1 and comprises a sequence of matrix-supported lithic-bearing pumice horizons and tuffs, capped with glassy obsidian which transitions into a jointed rhyolite flow (Fig. 4B). The obsidian and rhyolite show some flow banding and spatter textures (Fig. SI A3). The relative timing of this sequence and its relationship with the other units in the Southern Caldera Wall is difficult to delimit due to the absence of other recognised units. An interpretation of this sequence is outlined in Section 5.1.

3.3. Central caldera section (CC)

Systematic study of exposed sections (Site 15, 17, 18, 20 and 21) along the central caldera road (Fig. 2D) have revealed multiple, laterally persistent units (Table 4 & Figs. 7 & 8). Outcrops are commonly characterised by the presence of a large, diffusely bedded pumice deposit which occasionally grades into fine-grained ash (Figs. 7A & B). This unit is correlated to the Bedded Pumice unit outlined in (Fontijn et al., 2018).

A key feature of this unit is the reverse grading and staining from an overlying paleosol seen in the upper 0.3 m of the deposits. The consistency with which this lithofacies is observed made it a key marker for further correlations throughout the central caldera (Fig. 8A). The correlation of the Bedded Pumice Unit made here agrees well with previous authors (Fontijn et al., 2018; Rapprich et al., 2016), although Site 15 [MER001 of Fontijn et al., (2018)] has been updated after reassessment of the outcrop and its similarities with others in the stratigraphy. Overlying the Bedded Pumice Unit at multiple locations throughout the central caldera is a thin, obsidian-bearing, coarse-grained pumice horizon (CC_B). This latter unit and the Bedded Pumice provided the main stratigraphic makers for correlating units through the different sections within the central caldera and further correlation of deposits on the slopes of Urji.

Overlying CC_B is an ash-rich, lithic bearing PDC deposit containing a wide variety of clasts, including crystalline and flow banded rhyolite, obsidian, and pumice. At some localities, sparse ash aggregates are seen at the base of the outcrop. Units CC_D to CC_G (Figs. 7B & 8) are tentatively correlated with this deposit; however, they are described separately due to the difference in lithofacies. This sequence is subsequently overlain by a massive, well-sorted, obsidian-free pumice fall

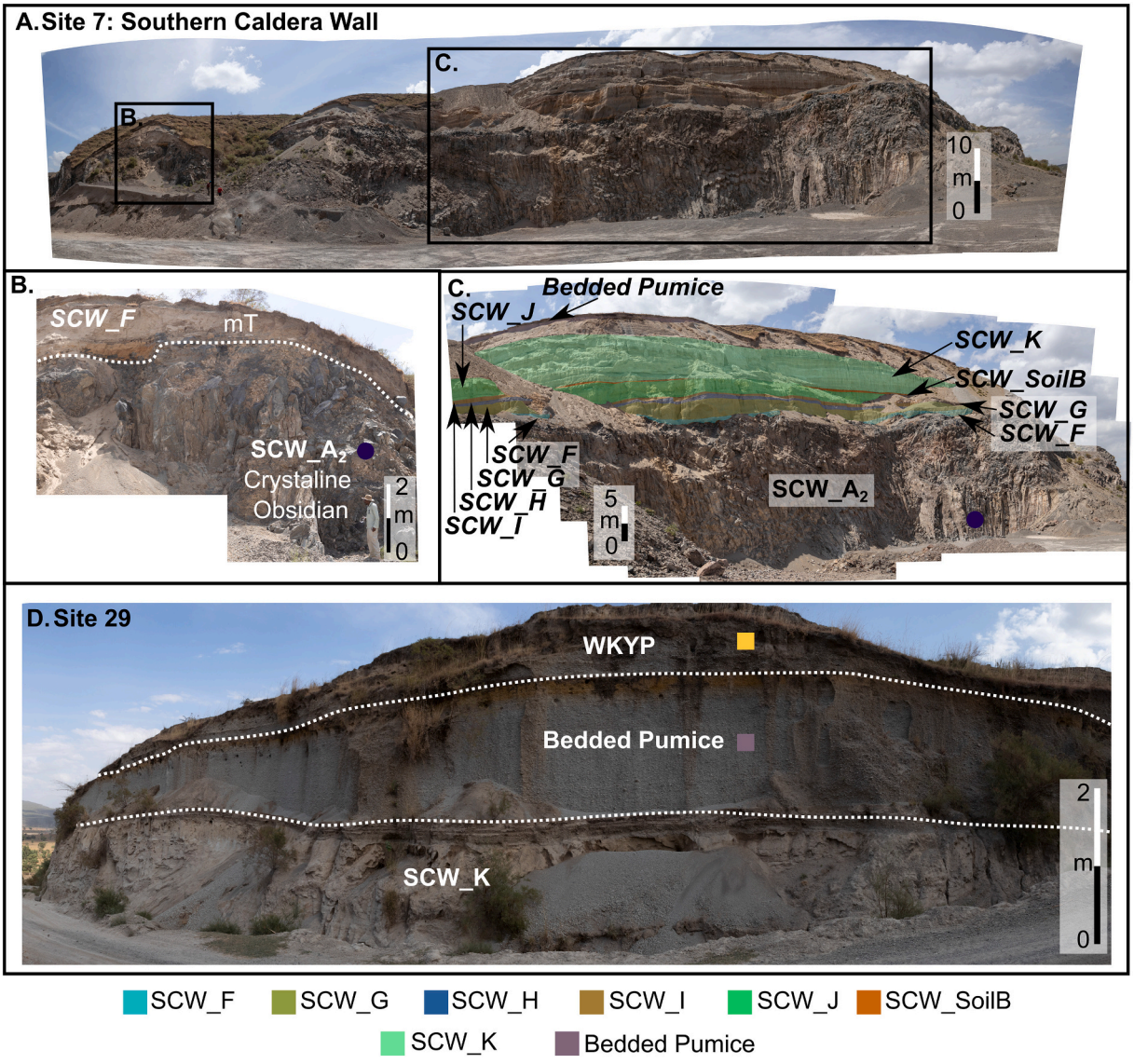

Fig. 5. A) Shows overview of outcrop at Site 7 (Fig. 2C) and location of panels B and C. B and C show details of the outcrop with C highlighting the major lithofacies observed (see Table 3). D) Outcrop at Site 29 (Fig. 2C) showing presence of Bedded Pumice and WKYP units capping the succession.

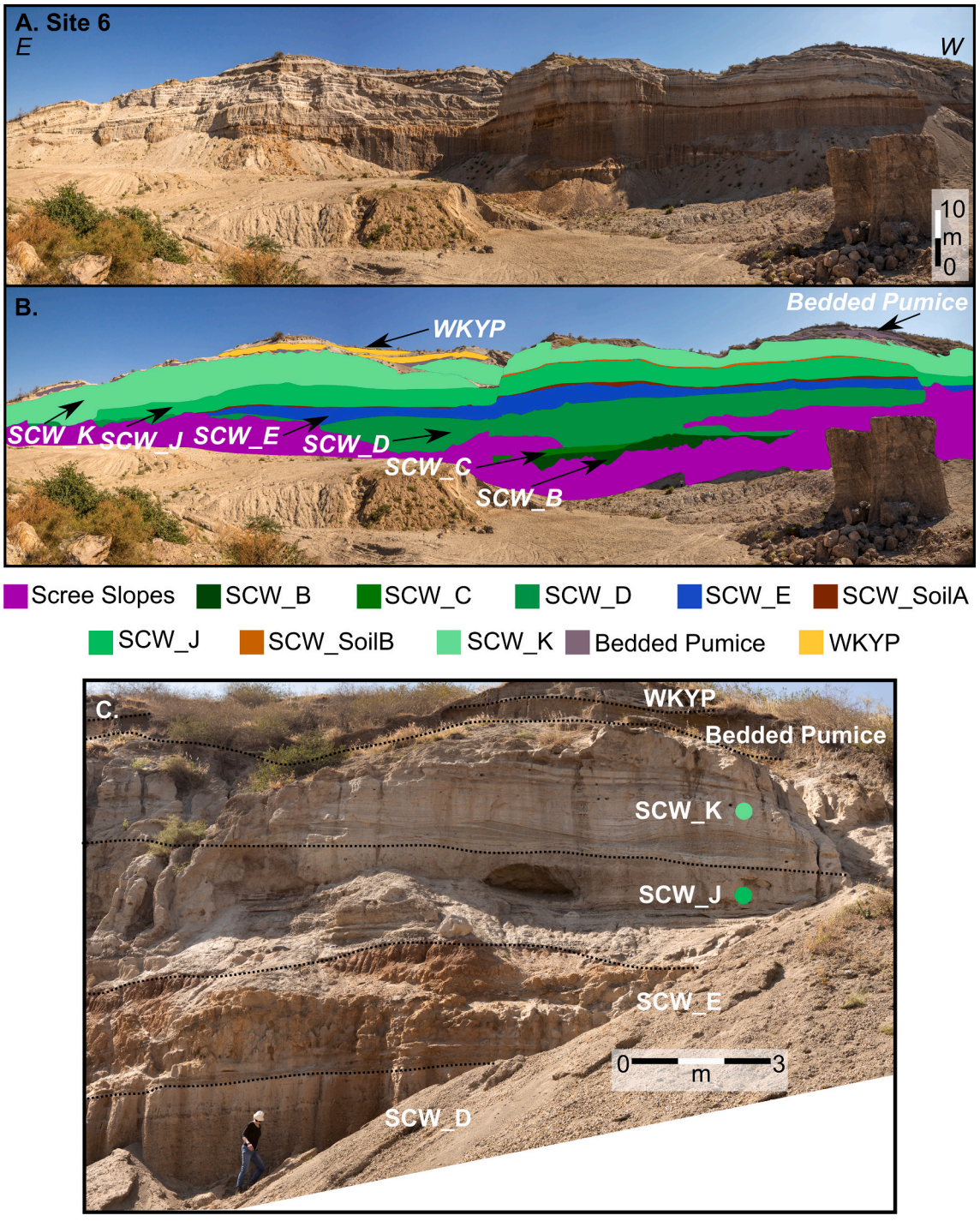

Fig. 6. A) Panoramic image of quarry in the southern caldera wall (Site 6, Fig. 2C) highlighting the identified units outline in Table 3 and Fig. 4C) Detail of the upper portion of the exposure which outcrops to the west of the panorama in A. Symbols denote location of samples.

deposit attributed to the WKYP eruption (Fontijn et al., 2018). The succession is capped by massive, obsidian bearing pumice fall deposits (CC_H).

3.4. Central gully (CG)

Outcrops in a gully off the main road through the caldera (Sites 40–44, 46; Fig. 2D) provide clear exposures of a succession of some of Corbetti's recent activity (Table 5, Figs. 8 & 9). At the base is an ash-rich tuff containing stratified pumice horizons (CG_A; Fig. 9A, C). Overlying this are two large pumice fall deposits (Fig. 9B–F). The lower pumice fall deposit displays diffuse stratification and clear flow packages of dilute PDCs (Fig. 9C). The top of this unit is stained by an overlying paleosol. We correlated this unit to the Bedded Pumice deposit due to its similarity in lithofacies and characteristic staining by overlying soil. Above this is a massive to diffusely stratified deposit attributed to the WKYP (Fig. 9B, D—F). Overlying the WKYP is a large obsidian lava deposit (CO5 [Rapprich et al., 2016]; Fig. 9E & F). This succession provides one of the few clear stratigraphic links between eruptive deposits of Urji and Chabbi, establishing the eruption of CO5 after the deposition of the WKYP unit. This has been key in incorporating Chabbi's relative chronology into the wider composite stratigraphy. At the top of the

Table 4
Description and interpretation of units exposed within the Central Caldera section as shown in Fig. 8. (See Fig. 2C for sample locations and Fig. 7 for field photos).

Unit	Type locality	LF	Thickness (m)	Description	Interpretation
CC_Soil_A	–	Soil	0.55	Topsoil containing some reworked pumice	Topsoil
CC_H	Site 15	mL	0.46	Massive clast-supported pumice deposit containing obsidian lithics (Fig. 7).	Pumice fall deposit only found at a single location, may be related to later eruptions of Chabbi and eroded from rest of caldera. Distinct from WKYP as unit is obsidian bearing
CO5	Site 17	Obsidian	8.43	Aphyric glassy obsidian	Lava flow from Chabbi
WKYP	Site 15	mL	1.87	Massive clast-supported pumice deposit (Fig. 7). Well sorted with some rare diffuse stratification observed at some localities. Lithics absent	Pumice fall deposit, bedding observed at some localities reflects proximal location to vent and slight variations in eruptive intensity.
CC_G	Site 15	dsLT	0.4	Coarse grained, poorly sorted, obsidian bearing, ashy matrix. Diffusely-stratified lapilli tuff (Fig. 7B)	Granular PDC
CC_F	Site 15	dsL/mT	0.7	Diffusely stratified tuff with horizons of stratified lapilli (Fig. 7B).	Fall deposit recording variation in eruptive activity at the vent allowing the generation of both pumice and ash.
CC_E	Site 15	sL/mT	1.1	Unit varies between stratified lapilli and massive tuff. Stratified lapilli are clast-supported which grades into finer-grained tuff. Pumice varied between 10 and 40 mm (Fig. 7B).	Either fall deposit with variation between pumice and ash reflective of changes in eruptive conditions at the vent, or records the deposition of several dilute PDC interbedded with pumice fall deposits.
CC_C	Site 17/18	maccBr / mlBr	2.75	Matrix-supported containing large pumice and lithic clasts. Lithic composition is highly varied, with banded and crystalline rhyolite present ranging in size between 10 and 400 mm. The base of the unit is ash-rich and contains sparse ash aggregates, most likely accretionary lapilli (Fig. 7C).	Dilute PDC. Eruption entrained material from the conduit. Accretionary lapilli suggest some degree of water interaction during the eruption. Uncertain if pumice is juvenile or remobilised.
CC_B	Site 21	mL	0.88	Coarse-grained pumice lapilli, clast supported containing obsidian lithics. Sparse highly vesicular pumice clasts were found, however they do not appear to have any clear stratigraphic placement. Pumice clasts range in size between 10 and 50 mm. Relatively poorly sorted (Fig. 7C).	Thin pumice fall deposit commonly observed above the Bedded Pumice deposit throughout the central caldera.
Bedded Pumice	Site 15/ 17/18/20	dsL	6.6	Diffusely stratified (on the order of ~0.1 m) pumice deposit. Clast-supported angular pumice ranges between 5 and 20 mm. The deposit contains sparse obsidian lithics dispersed throughout. The top ~0.3 m shows reverse grading and is stained by an overlying paleosol. Some outcrops have ash-rich horizons before transitioning to fine-grained reversely graded pumice (Fig. 7B & C).	Pumice fall deposit correlated with the Bedded Pumice units of Fontijn et al. (2018). Diffuse bedding reflects variation in eruptive conditions at the vent. Reverse grading in-upper 0.3 m reflects changing eruptive conditions at the vent (Duffield et al., 1979). Displays features of pumice cone eruption (Clarke et al., 2020).

succession is an ash-rich tuff showing some stratified lapilli (CG_E). Although there is no contact between CG_E and CO5, its absence underlying the lava suggests it overrode CO5 and has subsequently been eroded (Fig. 9G, H).

3.5. Urji slopes (US)

Multiple vents have been identified on the slopes of Urji (Hunt et al., 2019) however exposures are limited, therefore, we focus on the most recent activity associated with the Wendo Koshe Cone (Fig. 2F & Fig. 10; Table 6). Near the edge of the Urji edifice (Site 21 Fig. 2F), the base of the succession is large, jointed rhyolite lava (US_A; Fig. 10E; Table 6), which grades to glassy obsidian at the top. Numerous other lavas are recorded on the flanks of Urji, which are associated with older vents on the edifice (Fig. 2A) and buried by younger deposits.

At proximal locations on the flanks of the Wendo Koshe Cone (Sites 21 and 35 Fig. 2F), outcrops provide an insight into the cone's formation. The characteristic succession of the Bedded Pumice Unit overlain by a coarse-grained pumice horizon (CC_B) is repeated on the flanks of Urji at Site 21 (Fig. 10A, B). A second outcrop at Site 35 (Fig. 2F) reveals a coarse-grained, lithic-rich horizon (US_C) overlain by the Bedded Pumice unit (Fig. 10B). The WKYP deposit is absent on the flanks of the Wendo Koshe Cone.

To the north of the Wendo Koshe Cone, the distal deposits of the Bedded Pumice and WKYP are observed in a small gully. At the base of the succession, multiple ash-rich, pumice bearing horizons are identified (US_B). This unit has previously been identified by Rapprich et al. (2016) and attributed to phreatomagmatic activity. It is overlain by a diffusely stratified pumice fall deposit which is stained by a paleosol. It was previously termed the WKPO deposit by Rapprich et al. (2016) however, it shares the characteristic reverse grading and staining in the upper 0.3 m of the deposit seen in the Bedded Pumice unit and has therefore been correlated with it. It is likely covered by an outflow sheet linked with the collapse of the Wendo Koshe Cone and an associated obsidian lava flow, which outcrops on top of this flow. Clear outcrops of this succession could not be found.

3.6. Chabbi and the Biftu Tuff Cone

Chabbi is a large shield volcano that sits in the eastern portion of Corbetti Caldera (Fig. 2A). It consists of obsidian lavas erupted from numerous vents across the edifice and multiple pumice/tuff cones. Fig. 11 presents a relative chronology of the formation of different vents, pumice cones and the emplacement of the obsidian lavas. It incorporates findings of previous studies (Hunt et al., 2019; Rapprich et al., 2016) and observations from this study using a high-resolution DEM (Hunt et al., 2019). This chronology is based upon exposures seen at the surface today, and it is anticipated multiple other eruptions occurred across this edifice, the deposits of which are now buried.

Following the caldera-forming eruption (Fig. 11A) and the initial development of the edifice, activity at Chabbi was dominated by the formation of pumice cones on the northern flank (Fig. 11B-D). The pumice cone highlighted in Fig. 11B is the most heavily eroded and inferred to be the oldest exposed cone, with many of its deposits buried by subsequent activity. The cones highlighted in Fig. 11C and D have more extensive deposits and are inferred to be slightly younger, although no absolute chronology can be established. Following the development of these pumice cones, the first (CO3) of the four major obsidian lavas was emplaced. This deposit covers most of the northern flanks, with multiple lobes observed. One area of uncertainty surrounds the relative timing of the multiple buried lava flows and pyroclastic fans seen on the eastern flank and outside the caldera wall (Fig. 11E and F). These may be associated with other vents which have been covered by later deposits.

Following the emplacement of CO3 (and the likely eruption of other lava flows on the southern and eastern flanks), two pumice cones formed, named the Hot Cone and Eastern Cone by Mohr (1966) (Fig. 11G). The Hot Cone is the source of the next large obsidian deposit (CO4) recognised on Chabbi, CO4. Previously, the obsidian lavas on the eastern flank of Chabbi (Fig. 12) have been attributed to multiple eruptions from two vents (The Hot Cone and Eastern Cone of Mohr, 1966) and, more recently, to a single flow (CO4; Hunt et al., 2019; Rapprich et al., 2016). However, further investigation of the surface

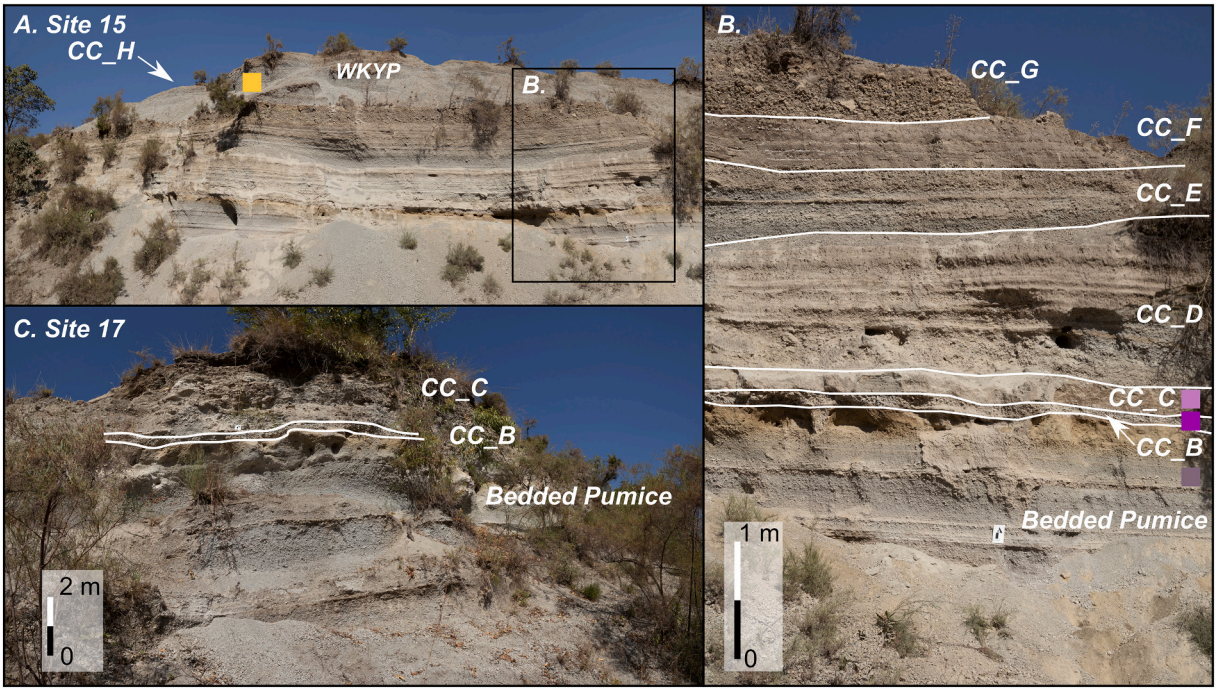

Fig. 7. Selected outcrops in the Central Caldera (Fig. 2D) highlighting the presence of key units outlined in Fig. 10 & Table 4. A-B) Site 15 (MER001 of Fontijn et al., 2018) overview and detail of major units. C) Site 17 showing the Bedded Pumice horizon and the consistent staining of the upper portion of the unit. Symbols denote the location of samples analysed in later sections.

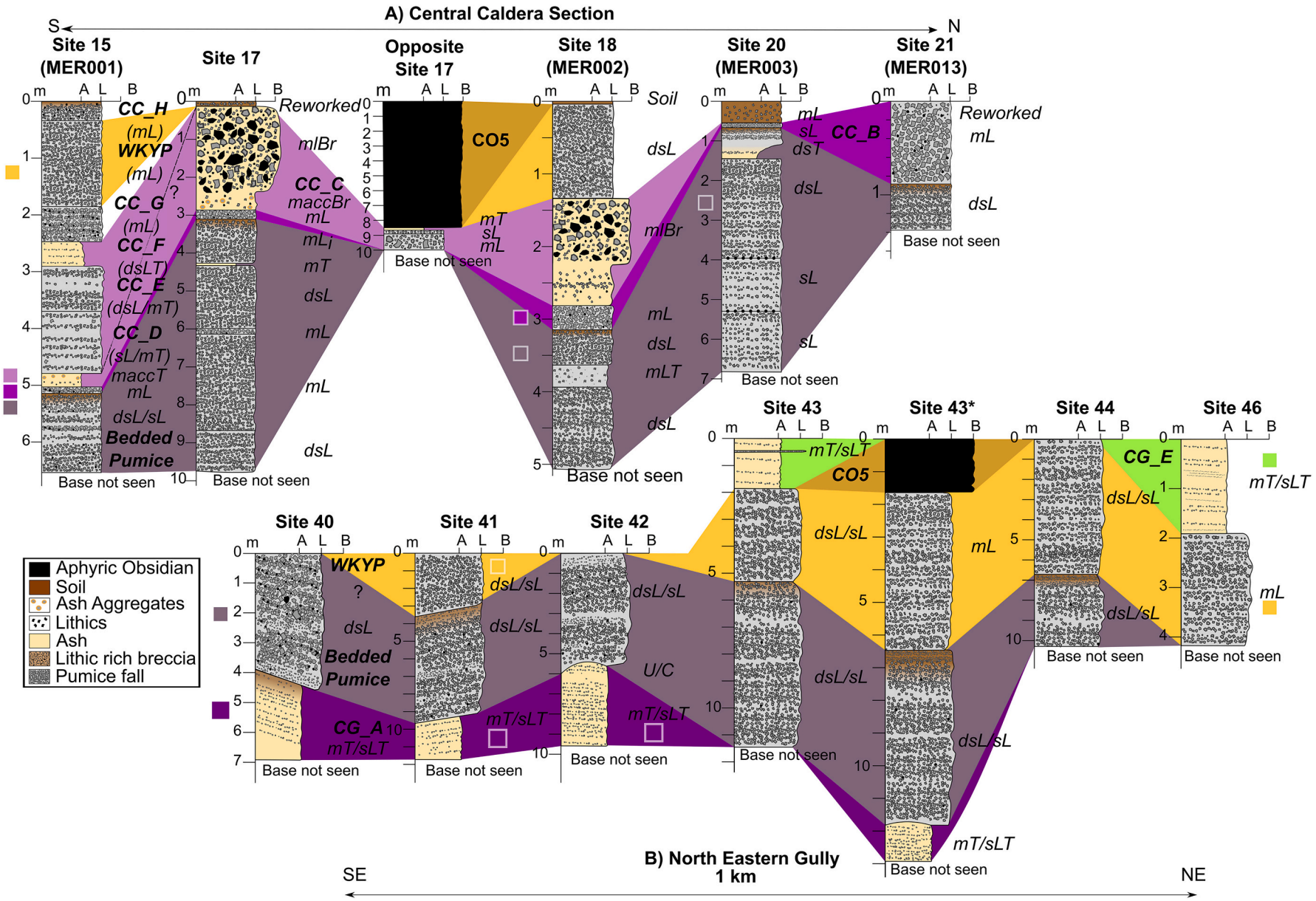

Fig. 8. A) Selected stratigraphic logs for outcrops in the Central Caldera (Fig. 2D) highlighting the major correlations (Table 4). B) Stratigraphic logs of outcrops in the north-eastern gully (Fig. 2E) with highlighted correlations based upon lateral tracing of units (Table 5). Symbols denote location of analysed samples.

Table 5
Description and interpretation of observed units in the north-eastern gully (Fig. 2E) Stratigraphic log is presented in Fig. 8B and field photos in Fig. 9.

Unit	Type locality	LF	Thickness (m)	Description	Interpretation
CG_E	Site 46	sT/ sLT	1.97	Stratified tuff to stratified lapilli tuff with lenses of coarse-grained pumice. Very fine-grained ash with pumice ranging in size between 5 and 20 mm (Fig. 9D, G & H)	Dilute PDC
CO5	Site 43	Lava	>1.68	Aphyric obsidian lava flow, unit likely thicker however only flow front observed (Fig. 9E & 9G)	CO5 obsidian lava from Chabbi
WKYP	Site 43	dsL/ mL	4.95	Well-sorted, clast-supported pumice deposit. Minor diffuse stratification in places but mostly massive. No lithics (Fig. 9A-F)	Proximal pumice fall deposit. Some diffuse stratification suggests periods of slight variation in eruptive activity
Bedded Pumice	Site 43	dsL	5.51	Well-sorted, clast-supported pumice deposit. Diffuse bedding was observed throughout. Staining at the top from overlying paleosol that is no longer present. Some localities show reverse grading in the upper 0.3 m of deposit (Fig. 9A-F)	Pumice fall deposit interbedded with ash-rich packages indicating the passage of dilute PDCs reflecting a highly unsteady eruption. Bedding reflects changes in eruptive condition at the vent. Some bedding features could also result from reworking of the deposit as it was deposited over paleo topography
CG_A	Site 42	sT/ sLT	6	Ash-rich tuff with clear stratification and horizons of stratified lapilli. Sparse lithics. Pumice ranges in size between 5 and 10 mm (Fig. 9A)	Dilute PDC with coarser lenses of pumice clasts.

morphology and elevation changes away from the Hot Cone vent suggests this unit comprises two different lavas from two vents. Fig. 12B shows elevation change along a profile of the CO4 lava. The elevation change is consistent with a flow moving away from the Hot Cone which is supported by the presence and direction of ogives on the surface of the flow. However, an abrupt change in elevation is seen ~900 m from the vent (Fig. 12B), where a ~ 25 m thick obsidian lava bisects and overlies CO4 (Fig. 12A) and is here termed CO4a. The drop in elevation seen around ~1750 m along the profile indicates the eastern extent of CO4a and the lava deposit past this point is likely the lower sections of CO4. This portion of the flow covers the flanks of the Eastern Cone, suggesting CO4 post-dates the formation of the cone. The surface morphology of CO4a indicates it flowed to the north and south, and ogives on the surface of the flow radiate out from a central point above the eastern cone, suggesting this is the source of the eruption, and it erupted through CO4. Pumice underlying CO4a has been $^{40}Ar/^{39}Ar$ dated to 19 ± 15 ka (Hutchison et al., 2016a).

It is inferred that the Biftu Tuff Cone, a rhyolitic tuff cone outside the caldera walls, formed after the emplacement of CO4a (Fig. 2). The formation and collapse of this cone resulted in the emplacement of a large, ash-rich pyroclastic density current (Clarke, 2020). Outcrops of these currents have been recorded on the eastern shore of Lake Hawassa by Clarke (2020) and in drainage gullies on the north-western shore in this study (Fig. 2H). The outcrops are dominated by a dilute, ash-rich PDC (Fig. 13A-F), which displays highly variable lithofacies along the length of the drainage gully with complex mm-scale sedimentary structures (Fig. 13B, C & E) to large meter scale bedforms (Fig. 13F). The deposit is dominated by ash, however, some coarse pumice-rich lenses are seen in large chute and pool bedforms. These pumice clasts typically range from ~1 mm to 25 mm and are highly rounded. Clasts of fine-grain ash are also incorporated into the deposit. The base of the PDC contains reworked/remobilised shells of *Melanoides tuberculata* as well as other gastropods and bivalves, indicating a degree of interaction with lake sediment during eruption and deposition. ^{14}C Dating of two *M. tuberculata* shells collected from within the PDC deposit yielded ages of 7375 ± 54 cal BP (Site30A1) and 7131.5 ± 121.5 cal BP (Site 30A2; Fig. 2H and Table 7). The dates and the $\delta^{13}C$ and $\delta^{18}O$ measurements match well with other samples of similar ages from Lake Hawassa, suggesting the shells were deposited during the wetter period in the rift before the transition to a more arid environment occurred around ~5130 cal BP (Lamb et al., 2002).

The succession above the PDC deposit is highly variable throughout the gully due to the partial collapse of the walls obscuring outcrops. At Site 12 (Fig. 2H), the PDC is overlain by thin horizons of ashy sediment, likely lake sediment, which is subsequently overlain by a coarse-grained pumice horizon containing abundant shells and rounded pumice clasts (Fig. 13A). Two shells from this unit were ^{14}C dated and yielded ages of 7751 ± 78 cal BP (Site 12C1) and 7779 ± 50 cal BP (Site 12C2; Table 7). These ages are significantly older than those determined for shells from the underlying PDC deposit. The stratigraphic sequence observed within the gullies (Fig. 13A) clearly shows the shells from Site12C overlying the Biftu Tuff PDC. The 'upside down' age sequence is likely the result of reworking and is discussed further in Section 5.2.1. The sequence is capped by a pumice fall deposit (Fig. 13B & D) however it is not visible at all locations along the gully. It has been correlated with the WKYP unit based on its stratigraphic position, lithofacies (mL) and the absence of obsidian lithics, a key characteristic of the deposit (Fontijn et al., 2018).

Following the emplacement of the WKYP, activity on Chabbi centred on the western flanks. One area of uncertainty is the timing and origin of the pyroclastic deposits on the western flanks of Chabbi (Fig. 13I). These deposits are partially buried by CO5, which makes up the majority of the western flanks. CO5 overlies the WKYP deposit indicating it erupted <2301 ± 120 cal BP (Rapprich et al., 2016). At the flow front of CO5, examples of ~1–2 m thick ~9 m long lenses of welded material are seen (SI A4). This pale, fine-grained material is seen to be intermingled with

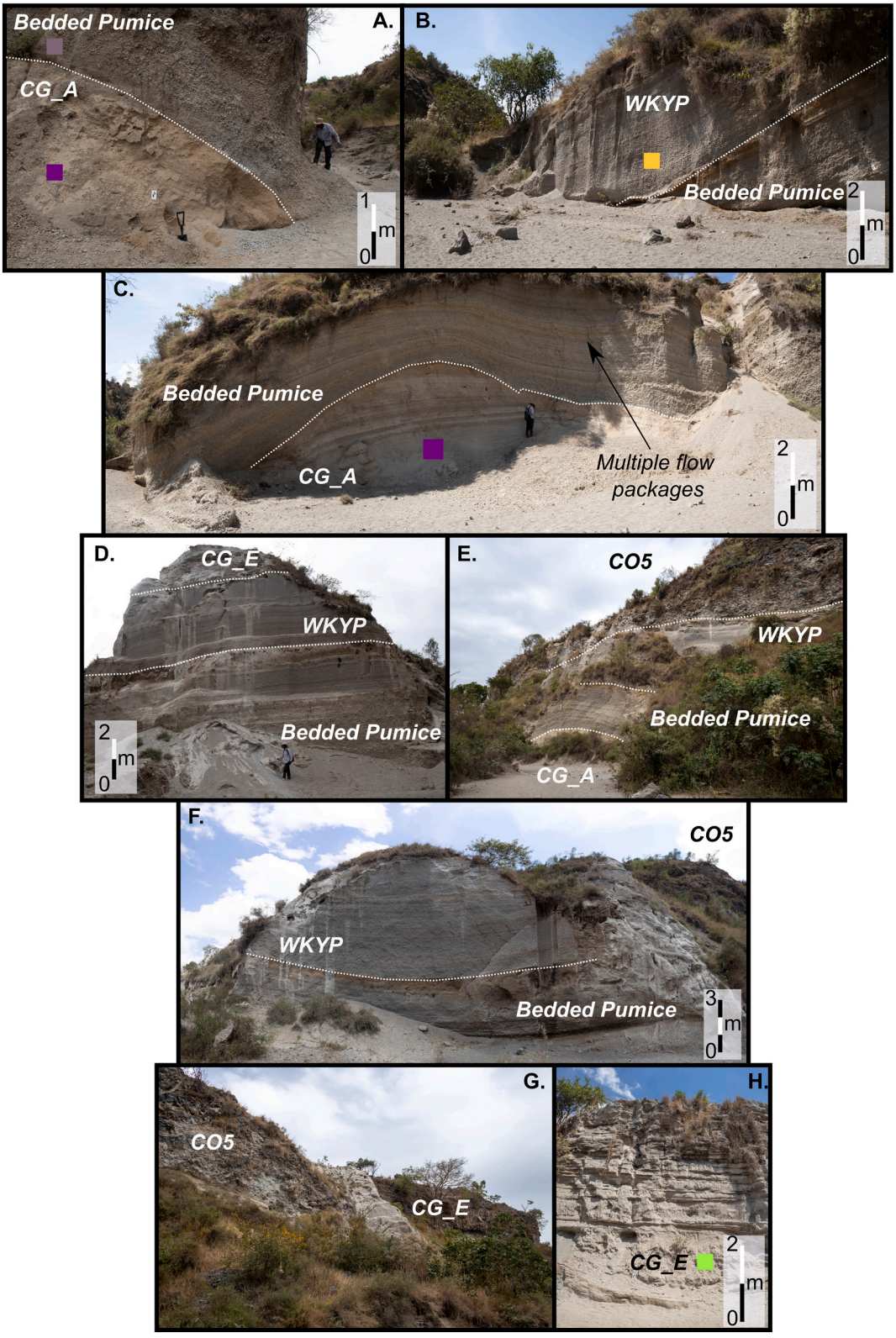

Fig. 9. (Above) Field photos from Sites in the central gully section of the caldera highlighted in Fig. 2E. A) Site 40, Bedded Pumice unit overlying an ash rich deposit. B) & C) outcrops at Site 41 of the WKYP and Bedded Pumice unit overlying ash-rich horizon. Slumping features observed. D) Large outcrop of Bedded Pumice and WKYP units capped with an ash rich PDC at Site 43. E) Outcrop opposite Site 43 showing contact between WKYP and CO5. Absence of CG_E suggests it was deposited after CO5. F) Shows characteristic features of the Bedded Pumice unit and WKYP overlain by CO5. G) Shows deposit of CG_E overlying CO5. H) Dilute ash rich PDC deposit (CG_E) comprised of multiple flow packages with sparse lithics and pumice clasts.

Table 6
Descriptions and interpretation of units observed on the slopes of Urji (Fig. 2F; logs and field photos presented in Fig. 10).

Unit	Type locality	LF	Thickness (m)	Description	Interpretation
WKYP	Site 38	mL	3	Massive to diffusely stratified, clast supported pumice deposit. Pumice ranged in size between 10 and 50 mm. Well sorted with sparse larger clasts (Fig. 10D)	Pumice fall deposit associated with the eruption of the Wendo Koshe Cone. Eruption likely culminated with the collapse of the cone and emplacement of the outflow sheet identified by Rapprich et al., (2016).
Bedded Pumice	Site 38	dsL	6.44	Diffusely stratified, on the order of ~10–200 mm, lapilli horizon. Clast supported, angular pumice lapilli ranges in size between 5 and 30 mm. Top ~0.4 m are stained by an overlying paleosol. However, paleosol is not visible as a distinct horizon (Fig. 10A-D)	Proximal pumice fall deposit associated with the formation of the Wendo Koshe Cone. Stratification and localised flow packages suggest highly unsteady eruption. Facies similar to those described by Clarke et al. (2020)
US_C	Site 35	mlL	1.85	Coarse-grained pumice and lithic rich horizon. Some pumice and lithics show signs of hydrothermal alteration. Lithics blocks up to 0.5 m seen. Very poorly sorted (Fig. 10C)	Proximal pumice fall deposit which has undergone post-deposition hydrothermal alteration. Records the highly energetic initial phases of the eruption which formed the Wendo Koshe Cone
US_B	Site 38	mT/ mL	2.53	Ash-rich unit with pumice rich horizons. Pumice clasts range from 10 mm to 0.2 m. Poor sorting (Fig. 10B)	Dilute, ash-rich PDC interbedded with pumice fall horizons. Coarse pumice-rich horizons indicate changes in the flow conditions within the current. Rapprich et al. (2016) inferred a phreatomagmatic origin.
US_A	Site 66	Lava	10	Aphyric jointed rhyolite which transitions towards glassy obsidian towards the top of the outcrop (Fig. 10E)	Rhyolitic lava from Urji. One of several which record the initial phases of activity at Urji

the obsidian glass at the edge of the lens (SI A4C). Some of the internal structure of the flow is also exposed in portions of the flow front, showing folding of the obsidian glass SI A4B). Investigation of the surface morphology of CO5 has revealed the presence of distinct units which have previously been attributed to CO5. Two lavas overlie CO5 and are associated with two vents identified by Hunt et al. (2019), which we call CO5a and CO5b (Fig. 11K). The most recent flow on Chabbi, CO6, covers the southern flank. It is sourced from a single vent with multiple lobes overriding earlier portions of the flows. Observed outcrops of the CO6 lava show it to be glassy, crystal-free obsidian. An outcrop at Site 58 (Fig. 2C) shows a pale lens of welded material similar to that observed in CO5 (SI A4D).

4. Geochemistry

4.1. Major element geochemistry

Fig. 14A summarises the compositions of rock samples on a total alkali-silica diagram. The legend in the geochemical plots remains consistent throughout unless otherwise stated, and the sample locations are highlighted in field photos and stratigraphic logs. The major element data shows very little variation in composition between erupted magmas, supporting previous observations (Fontijn et al., 2018; Martin-Jones et al., 2017). Most samples are rhyolitic with sparse trachyte samples.

All but two samples have a peralkalinity index (Pl = molar $Na_2O + K_2O/Al_2O_3$; Shand, 1927) between 1 and 1.5. These samples can be further divided into pantellerites and comendites based upon the relative concentration of Total Iron and Al_2O_3 (Fig. 14B; MacDonald, 1974). Peralkaline samples from Corbetti span the comendite-pantellerite boundary with samples from pre- and post-caldera activity recording both compositions. Whole rock and glass compositions of Corbetti samples from Rapprich et al. (2016) and Fontijn et al. (2018), respectively, are also presented for comparison in these figures.

4.2. Trace element geochemistry

Fig. 15 shows selected incompatible trace elements plotted against Zr, which is used as a proxy for fractional crystallisation because it behaves incompatibly across our sample set. The lack of mafic and intermediate compositions means the majority of the sample set reflects late-stage crystallisation characterised by depletion in Sr and Ba due to the crystallisation of alkali feldspars. Incompatible-incompatible element diagrams (Y, La, and Rb against Zr) show a clear positive trend, consistent with fractional crystallisation. The trends seen within these data are consistent with previous studies that found peralkaline magmas undergo >90% fractional crystallisation to reach these compositions (Gleeson et al., 2017; Macdonald et al., 2012; Peccerillo et al., 2007; White et al., 2009). These data demonstrate that whilst there are some variations between pre-and post-caldera deposits, distinguishing between units based upon their geochemical composition is challenging (SI A5).

5. Discussion: eruptive history of Corbetti Caldera

By integrating our new field observations with previous authors' findings, we develop a composite stratigraphy of Corbetti Caldera. Fig. 16 outlines this compiled composite stratigraphy and includes units of uncertain stratigraphic placement. Our findings support previous observations that activity at Corbetti has ranged from eruptions generating extensive rhyolitic and obsidian lavas to the generation of multiple ash-rich pyroclastic density currents and Plinian-style fall deposits. We also find evidence for previously undocumented eruptions which suggest Corbetti has undergone multiple phases of large-scale explosive activity which may have resulted in the partial or full collapse of edifices within the complex. Whole-rock geochemical analysis (Figs. 14 & 15)

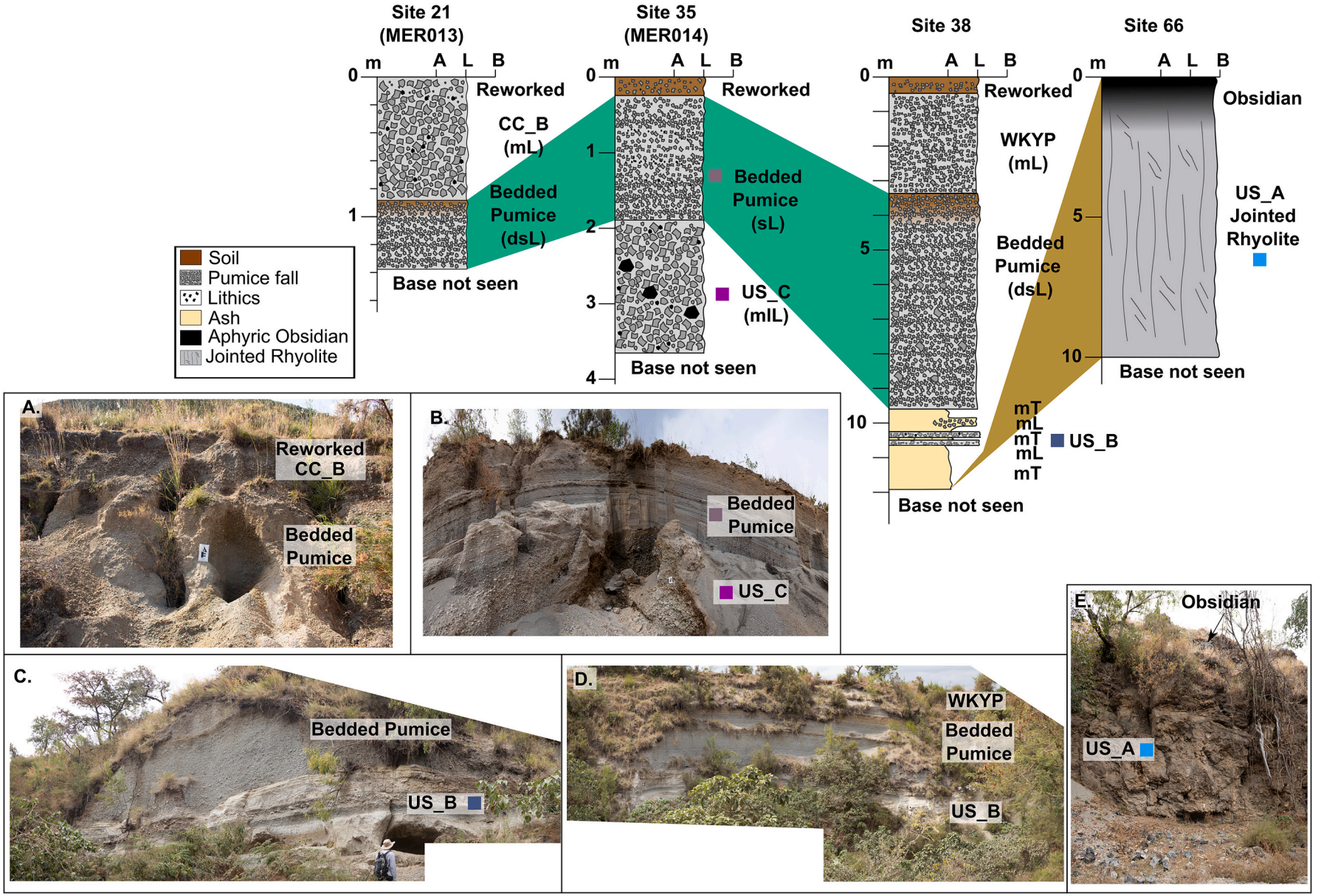

Fig. 10. (Above) Stratigraphic logs from locations on and around the flanks of the Wendo Koshe Cone of Urji. Sample locations are highlighted in Fig. 2F and units are described in Table 6. A) Outcrop on the flanks of the Wendo Koshe Cone (Site 21) showing the Bedded Pumice unit with the characteristic reverse grading and staining by overlying paleosol. This is overlain by the coarse-grained, obsidian bearing pumice fall deposit seen at numerous locations in the central caldera (CC_B; Fig. 8) B) Outcrop on the flanks of the Wendo Koshe Cone showing proximal deposits characteristic of a pumice cone eruption. C & D) Outcrops at Site 38 showing similar characteristics described in Rapprich et al. (2016). E) Rhyolite flow on the flanks of Urji which grades to glassy obsidian.

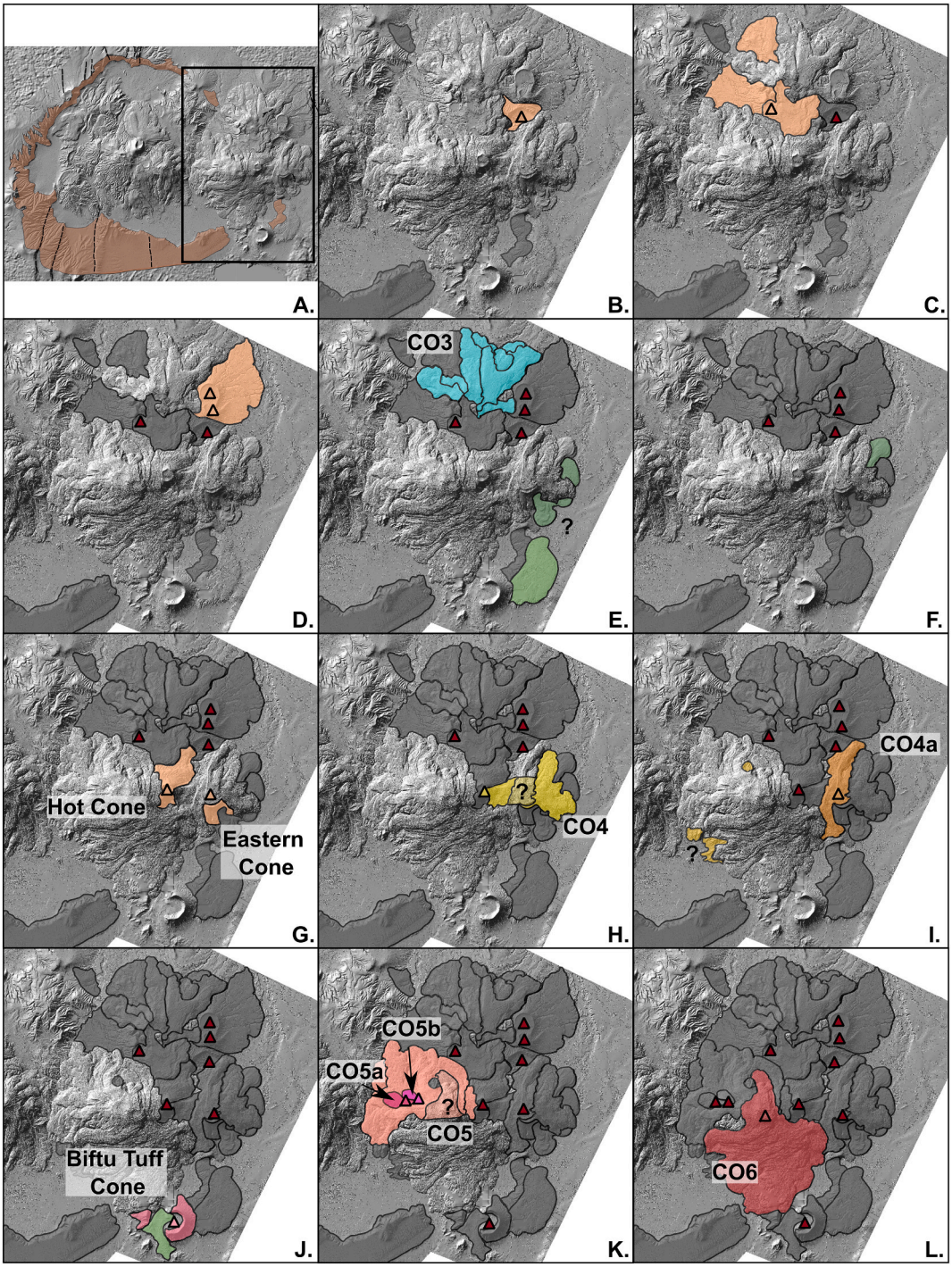

Fig. 11. Overview of our proposed development of Chabbi. A) Caldera forming eruption followed by the development of Artu, Urji and Chabbi. Box highlights Chabbi and region of subsequent maps. B-D) The most heavily eroded areas of Chabbi are associated with pumice cone eruptions forming multiple vents some of which overlap; however the relative timing of these eruptions is difficult to constrain. E) Eruption of CO3 from a now eroded vent. CO3 has multiple lobes which over-ride earlier portions of the deposit. The timing of the deposits on the south-eastern flank are thought to occur around this time however no dates for these eruptions are currently available. F) Lava flow from a now buried vent, ogives can still be seen on the surface of the flow although it has been subsequently buried. G) Further pumice cone eruptions forming the Hot Cone (central) and the Eastern Cone (right) of Mohr (1966). H) Eruption of CO4 which is inferred to have overridden part of the eastern cone. I) Eruption of CO4a from a vent near the eastern cone. This flow erupted through CO4. J) Eruption of the Biftu Tuff cone. Two vents are seen on the western flank of Chabbi however the timing of their formation is uncertain After (Clarke, 2020). K) Eruption of CO5 from a now buried vent. Following this eruption two other vents formed erupting small lava flows which are identified here for the first time and termed CO5a and CO5b. L) Eruption of CO6 from a central vent. This is the most recent flow on Chabbi and has multiple lobes which override earlier portions of the flow.

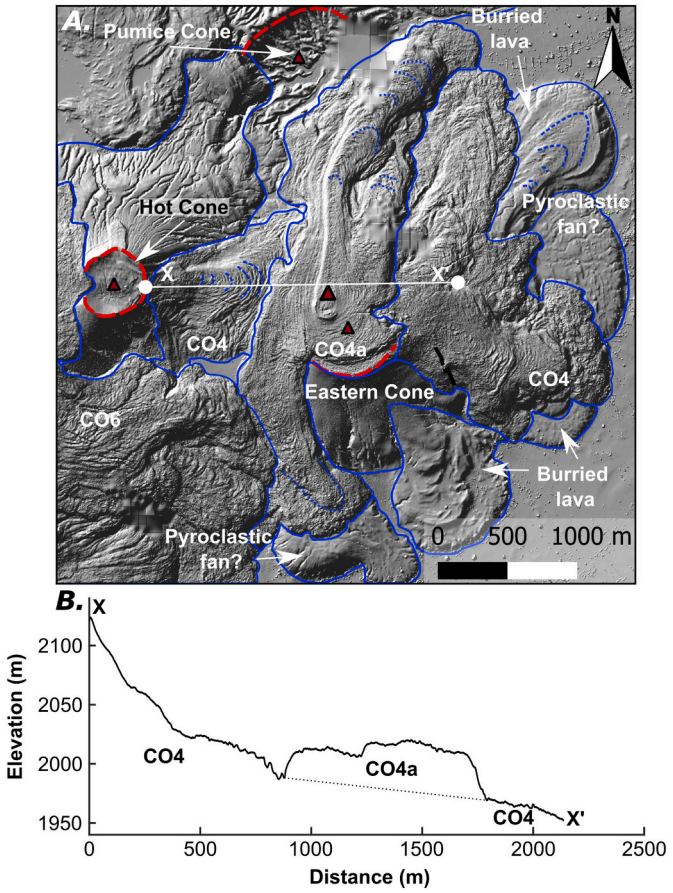

Fig. 12. A) Detail of the CO4 and CO4a (Fig. 13) showing the surface morphology of the two flows and surrounding features. Ogives visible in CO4a suggest the vent of the eruption is slightly offset from the eastern cone vent suggesting it is sourced from a different vent. In addition, the ogives on the upper portions of CO4 are clearly not altered by the presence of CO4a suggesting CO4a was emplaced later on top of CO4. B) Change in elevation along profile highlighted in A. The abrupt change in height highlights the presence of CO4a and provides further evidence for it being a separate flow.

shows Corbetti consistently erupts peralkaline rhyolites. Whilst some variation in geochemistry is observed, it occurs over a narrow compositional range (SI A5) and lacks the chemical diversity seen at other MER calderas (Fontijn et al., 2018; Iddon et al., 2019; Ronga et al., 2009; Rooney et al., 2012; Tadesse et al., 2019).

5.1. Early phases of activity

Early activity at Corbetti was characterised by the eruption of multiple rhyolite lavas, which are found both in the southern caldera wall (SCW_A_1 & SCW_A_2; Figs. 5 & 6) and the northern caldera wall (NCW_A; Fig. 3A). The eruption of these lavas resulted in the development of a low relief shield, which is typical of early evolution at other MER calderas (Hutchison et al., 2016b). The initial lavas likely erupted from distinct vents across several edifices instead of erupting from a single central edifice. We find evidence of spatially unique outcrops within the caldera wall, which have different lithofacies to surrounding areas. For instance, we infer that the outcrop at Site 8 (Fig. 2C & SI A3) records the deposits from a now eroded vent. The pyroclastic succession records the main phase of activity which generated PDCs and ejected obsidian ballistics before a transition to a spatter-like eruption of obsidian and rhyolite. The highly localised nature of this outcrop suggests it may originate from a proximal vent. It is common for large shield volcanoes to be polygenetic, especially in highly evolved systems (i.e., Pantelleria, Socorro), and frequently erupt pyroclastic cones (Grosse and Kervyn, 2018; Webb and Weaver, 1975). We suggest that whilst a central vent may have been present at Corbetti, eruptions occurred at multiple smaller vents across the pre-caldera shield, resulting in the highly localised deposits seen within the caldera wall today (i.e., Site 8; Fig. 2C). These vents' locations were likely influenced by pre-existing faults related to the initial stages of rifting.

Following an early shield building phase, many silicic centres within the MER underwent caldera-forming eruptions (Hutchison et al., 2016a, 2016b; Rampey et al., 2010). Recent work has highlighted the short timescales (decades to centuries) necessary to accumulate large magma bodies capable of feeding caldera-forming eruptions (Costa et al., 2020; Jackson et al., 2018). Within the MER, four caldera-forming eruptions (Aluto, Gedemsa, Shala Caldera and Corbetti) occurred in close temporal succession during the late Pleistocene. Hutchison et al. (2016a) linked these eruptions to an increased melt flux from a mantle-derived plume. This increased melt flux may have resulted in the remobilisation of parts of mid-crustal, highly evolved crystalline mush allowing a sizeable magma body to accumulate at shallow depths. The proposed small timescales over which this accumulation is possible would explain why four volcanoes underwent caldera-forming eruptions over a geologically short time. However, it is a common feature of the large silicic complexes within the MER to undergo this cycle of shield building followed by caldera collapse, and there are several examples of caldera-forming eruptions that have not been directly linked to an increase in mantle activity (i.e. Tullu Moye, Kone and Melkassa; Fontijn et al., 2018).

Corbetti is a fault-controlled caldera whereby the shape of the caldera links to the reactivation of pre-existing structures within the crust (Hunt et al., 2019; Maestrelli et al., 2022; Robertson et al., 2016). Whilst Corbetti has the morphology of a caldera, the eruption associated with caldera collapse is enigmatic. Previous studies have highlighted the presence of a welded ignimbrite outcropping above the jointed rhyolite lavas (Altaye, 1984) in the western caldera walls. This unit is interpreted as the deposits from a caldera-forming eruption and dates to ~182 ± 28 ka (Hutchison et al., 2016a; Vidal et al., 2022). Peralkaline complexes commonly produce welded PDC deposits, also from both smaller and larger eruptions, therefore, the presence of welded ignimbrites alone is not indicative of a caldera-forming eruption (Jordan et al., 2018; Mahood, 1984).

Here we find evidence of several deposits recording the deposition of welded (NCW_F) and non-welded (NCW_E) ignimbrites as well as lithic lag breccias (SCW_B & SCW_D) (Fig. 16). Determining the relative timing of these units in relation to the caldera-forming eruption is critical, as it may demonstrate a more complex caldera formation process than previously thought. However, due to a lack of suitable crystal phases, dating these units was not possible.

As outlined in Section 3.1, a red ignimbrite (NCW_E) outcrops within the North caldera wall and extends some 15 km to the east. It is the most widespread ignimbrite sheet observed at Corbetti and is likely associated with a large-scale eruption. This unit is overlain by a green welded ignimbrite containing obsidian fiamme (Fig. 3C-D). In addition, within the southern caldera wall, two lithic lag breccias are interbedded with thin dilute PDCs (Section 3.2; Fig. 6). These breccias are of particular interest as they are previously undocumented and exclusively outcrop at a single location (Site 6; Fig. 2C). Lithic lag breccias are often associated with large-scale collapse events and are commonly found within large caldera complexes (e.g., Druitt, 1985; Jordan et al., 2018; Simmons et al., 2016). They are often proximal to vents, contain compositionally diverse clasts and exhibit limited structures. The breccias observed at Corbetti match these criteria (Table 3). The key questions are whether any/all of the ignimbrite and lithic breccia deposits are linked to a/the caldera-forming eruption or record separate events/ phases of activity.

These units are either seen to, or inferred to, outcrop above the rhyolitic lavas. The lithic lag breccias in the southern caldera (SCW_B & SCW_D; Fig. 6) wall contain an abundance of red ignimbrite fragments, similar to the red ignimbrite (NCW_E) seen in the northern caldera wall.

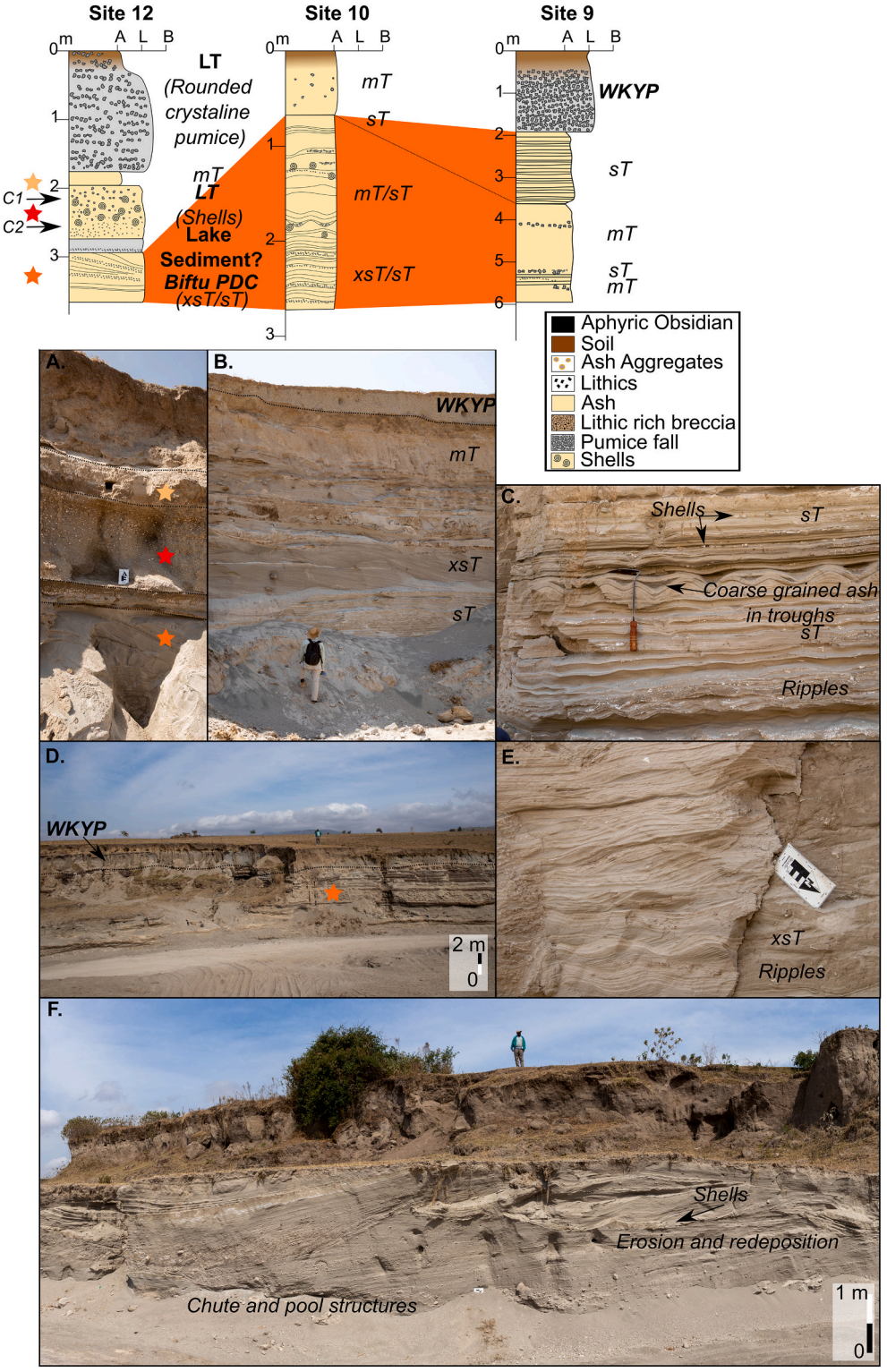

Fig. 13. Stratigraphic log and field photos of outcrops in a drainage gully near the shores of Lake Hawassa. Field sites are marked in Fig. 2H) Outcrop at Site 12 showing the upper portion of a dilute PDC with a shell-bearing horizon and lapilli tuff B) Outcrop at Site 31 (Fig. 2H) showing the complex and varied structures within the dilute PDC associated with the Biftu Tuff Cone C) Wave ripples and stratification observed at Site 10. Shells incorporated into deposit. D) Overview of Site 9 showing PDC succession caped with the WKYP. E) Complex cross stratification and ripples at Site 10. F) overview of Site 11 showing chute and pool structures and incorporation of shells into PDC.

No clasts of the green welded ignimbrite (NCW_F) are found within the deposit. This suggests two possible scenarios: (1) the breccias were emplaced before the red ignimbrite in the North Caldera Wall, remobilising a distinct ignimbrite horizon along with other lavas. (2) Breccias were emplaced during /after the eruption of the red ignimbrite sheet (NCW_E) but before the green welded ignimbrite (NCW_F) was emplaced. The absence of clear evidence indicating a second red ignimbrite within the caldera suggests the second scenario is more likely. Similarly, the absence of ignimbrites in the rest of the southern caldera and portions of the northern caldera wall may reflect a highly directional eruption, with most of the eruptive products travelling towards the east and subsequently being buried by Chabbi or eroded by later PDCs.

Based upon this evidence, we propose that the red ignimbrite (NCW_E) was emplaced by a large scale PDC which preferentially deposited to the north and northeast based upon observed exposures

Table 7
Radiocarbon dating and stable isotope results for shells sampled from the Biftu Tuff Cone PDC (Site30A) and overlying pumice deposit (Site 12C). Field sites are marked in Fig. 2H. Samples were analysed at Beta Analytic and calibrated using BetaCal4.20: HPD method: INTCAL20 (Reimer et al., 2020).

Sample	Material	Conventional age	Calendar calibration (cal BP)		Probability %	Stable isotopes (‰)	
		± 30 BP	Max	Min		$\delta^{13}C$	$\delta^{18}O$
Site12C1	Shell	6910	7794	7673	91.4	−1.4	3.15
			7829	7813	4		
Site12C2	Shell	6810	7685	7585	95.4	−2.7	3.12
Site30A1	Shell	6470	7429	7321	95.4	−3.1	3.97
			7130	7010	52.5		
Site30A2	Shell	6230	7253	7193	30.1	−3.5	3.61
			7176	7151	12.8		

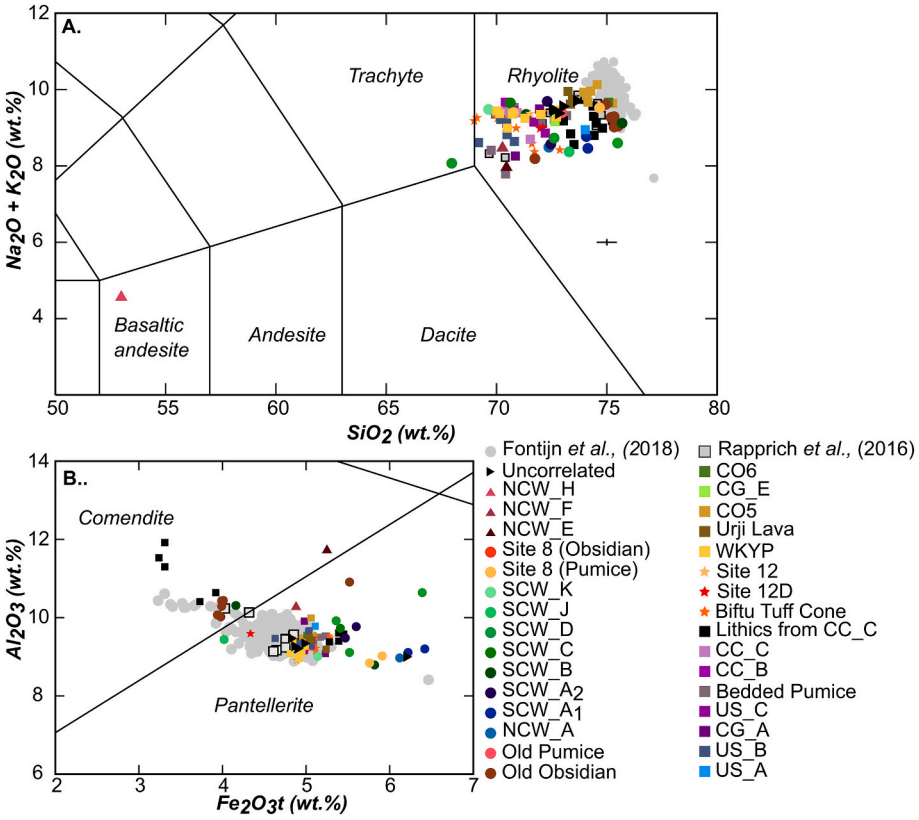

Fig. 14. A) Total alkali silica diagram highlighting the limited variation in erupted compositions from Corbetti. Samples were grouped based upon correlations outlined in previous sections. Error bar is calculated from the 2*RSD% of standard. Samples from Rapprich et al. (2016) and glass compositions from Fontijn et al. (2018) are shown for comparison. B) Peralkaline classification distinguishing between comendite and pantellerite composition using the divide proposed by MacDonald (1974). Errors smaller than symbols.

(see Section 3.1). This was followed by activity relating to the collapse of the edifice, which generated a large, granular PDC and remobilised significant portions of the previously deposited red ignimbrite. This PDC was strongly topographically controlled, depositing locally in a paleovalley in the modern-day southern caldera wall. Subsequently, a dilute PDC (SCW_C; Fig. 4B) was generated scouring out portions of the lithic breccia before a second, large-scale, granular PDC (SCW_D) was emplaced in the same paleovalley. This second current may be linked to the collapse of the edifice. The emplacement of the green welded ignimbrite (NCW_F; Fig. 3C & 4A) occurred after the deposition of the lithic lag breccias however it is uncertain if this occurred during the same phase of activity or was a distinct event.

We find numerous examples of fine-grained, ash-rich PDC deposits (e.g., SCW_J, SCW_K, NCW_H; Figs. 3E-G, 6). Due to limited exposures of these deposits, there is some uncertainty surrounding their relative timing (highlighted in Fig. 16). However, these deposits highlight the propensity for eruptions at Corbetti to continually produce large-scale, dilute PDCs which has significant implications for understanding the future hazard posed by its eruptions.

5.2. Post-caldera activity

Post-caldera activity at Corbetti has centred around three main edifices, Artu, Urji and Chabbi. Artu is the oldest observable post-caldera edifice and is situated close to the northern caldera wall (Fig. 2A). Little is known about its eruptive history as deposits have either been heavily eroded or buried by subsequent volcanism; however it is likely to have experienced pumice cone forming eruptions and associated eruption of lavas as is typical within the MER (Clarke et al., 2020, 2019; Hutchison et al., 2016b). Activity then focused around the two major edifices seen within the caldera today, Urji and Chabbi (Fig. 2A). These edifices formed through eruptions from numerous vents, which are strongly controlled by the W-E trending faults. (Hunt et al., 2019; Lloyd et al., 2018b). The formation of multiple new vents within a caldera is commonly observed at other MER volcanoes (e.g., Aluto; Hunt et al., 2019; Hutchison et al., 2016b), however, they tend to form on the edges of the caldera scarp likely controlled by the presence of ring faults and structural weaknesses caused by caldera collapse (Hunt et al., 2019). The fact that Urji has formed centrally within the caldera, and the vents on both Urji and Chabbi strongly align to the W-E trending faults

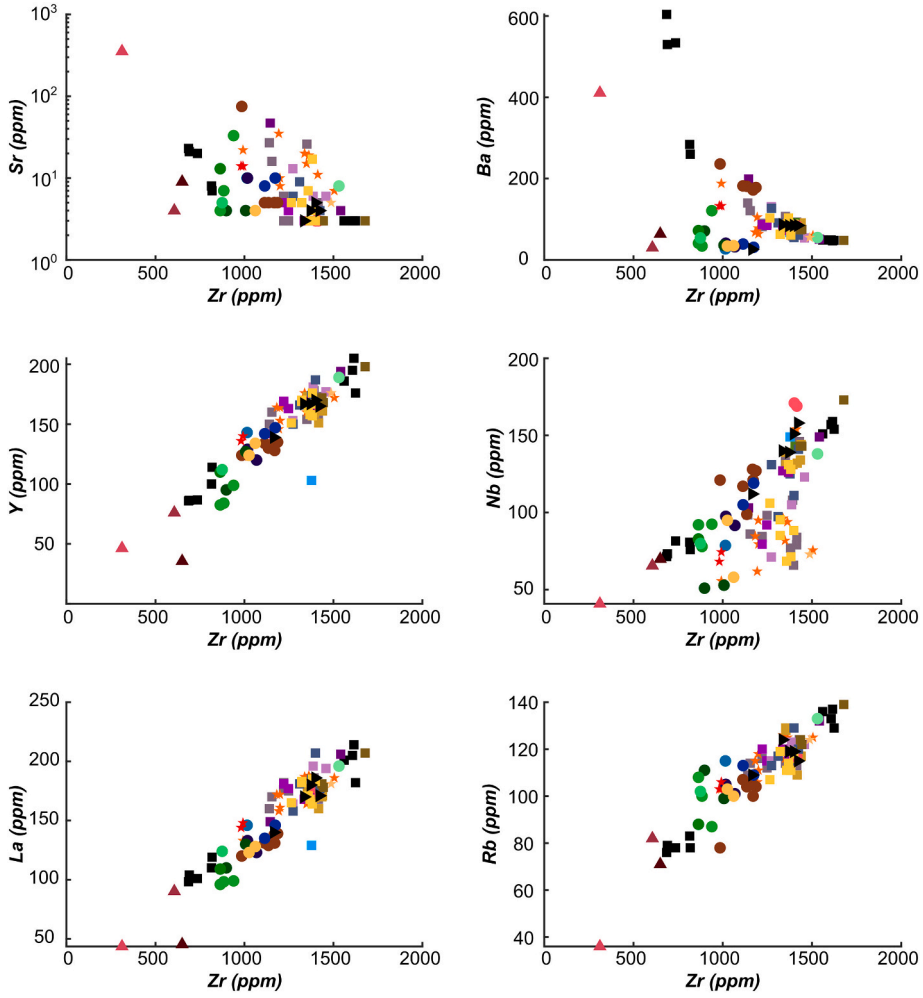

Fig. 15. Trace element plots for samples analysed in this study. Legend is the same as Fig. 15. Incompatible-incompatible (Y, Nb, La, Rb vs Zr) plots show a clear fractional crystallisation trend. Error bars smaller than symbols.

highlights the first-order control these pre-existing structures have on the locus of volcanism at Corbetti. This observation is especially significant when considering the location of any future volcanism at Corbetti.

The relative timing of the formation of Urji and Chabbi remains unclear, however evidence from the flanks of Urji demonstrates activity likely started with a shield building phase with the eruption of multiple rhyolite lava flows (e.g., US_A; Fig. 10) before a transition to pumice cone eruptions, which have dominated Urji's recent eruptive history. The early activity at Chabbi is unclear; however, the oldest observed are heavily eroded pumice cones on the north and northeast flanks (Fig. 11B-D). Buried lava and pyroclastic fans are also seen on the south-eastern flanks (Fig. 11E, 12). This activity style contrasts with recent eruptions, in which the emplacement of large obsidian lavas has dominated. The reasons for this transition from pumice cone eruptions to the eruption of extensive obsidian lavas require further investigation. Previous work has identified four major obsidian lavas (CO3, CO4, CO5, CO6) however, as presented in Section 3.6, we have delimited a further three lavas on the flanks of Chabbi (CO4a, CO5a and CO5b; Fig. 12). It is challenging to constrain whether these additional lavas are related to the eruptions that deposited the previously identified lavas or from different events. Evidence from the rest of the caldera suggests it is uncommon for a post-caldera eruption to form multiple vents, such as during basaltic fissure eruptions. Identification of these lavas indicates that Chabbi has been more active than previously thought.

As outlined in Section 3.6, we demonstrate that the obsidian deposit CO4 comprises two distinct lavas (CO4 and CO4a Fig. 12) which erupted from different vents. Here we infer a pumice cone eruption formed the Eastern Cone, followed by the eruption of the Hot Cone and emplacement of CO4. The vent from which CO4a erupted (Fig. 12) is offset from the central point of the eastern cone. We suggest a secondary vent opened on the northern flank of the eastern cone from which CO4a erupted. This supports previous findings which indicate vents are more likely to open in close proximity to the two pre-existing faults within the caldera and are more likely to form close to previous vents (Clarke et al., 2020; Hunt et al., 2019). This can have the effect of obscuring deposits or giving the appearance of a single vent and should be considered when assessing the source of eruptions. In addition, this is significant for assessing the probabilistic and spatial risk of new vents opening on the flanks of Chabbi.

In contrast to Chabbi, explosive eruptions generating widespread pumice fall deposits (e.g., Bedded Pumice and WKYP) and localised dilute PDCs (e.g., CC_D; See Section 3.3) dominate on Urji. Some of the earliest activity recorded on Urji is the deposition of several ash-rich PDC units, some of which (US_B; Fig. 10C) have previously been attributed to phreatomagmatic activity (Rapprich et al., 2016). Previous work has suggested the presence of a lake within part of the caldera, likely during a high stand period of Lake Hawassa (Altaye, 1984; Lamb et al., 2002) however further investigation into this is required. One important observation is the scarcity of these PDCs at distal locations outside the caldera walls indicating flows are unlikely to have large runout distances however, future similar PDC-generating eruptions

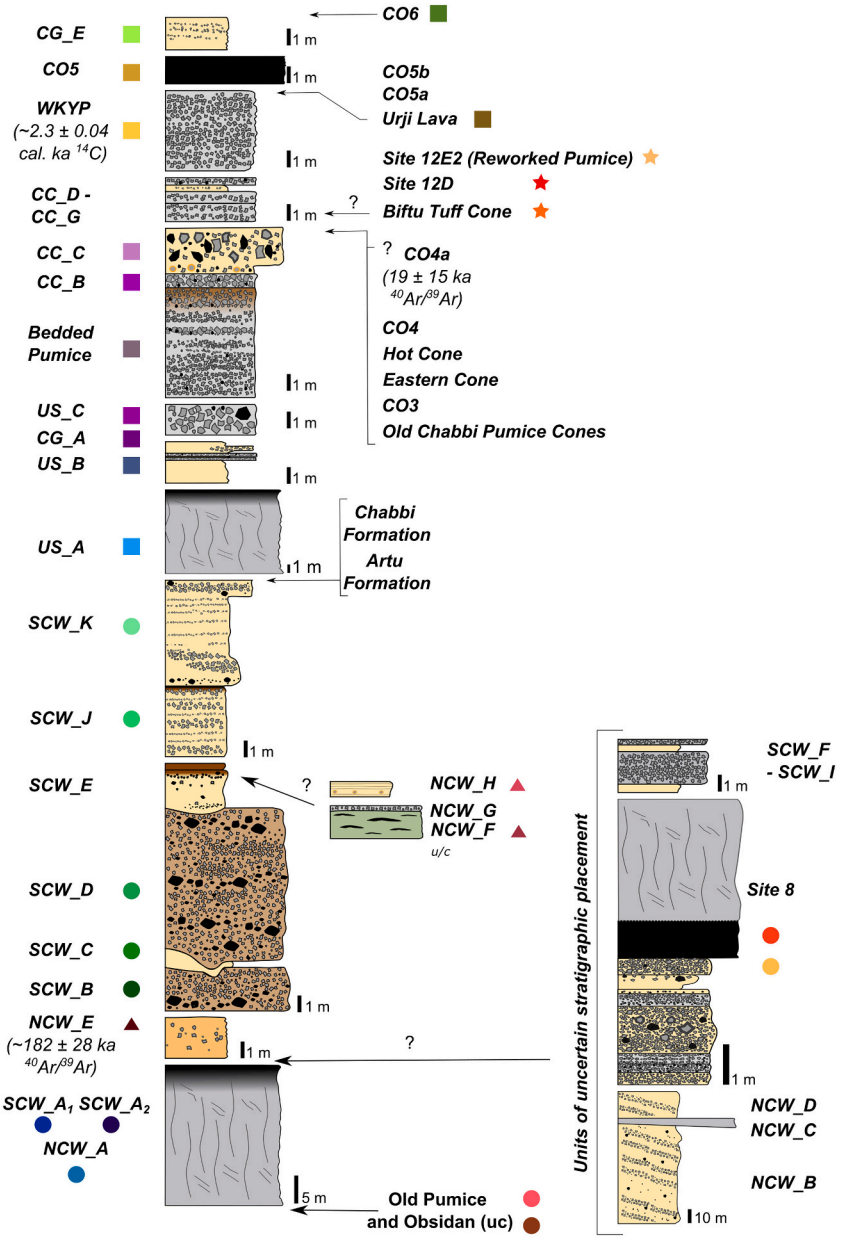

Fig. 16. Composite stratigraphy of Corbetti Caldera Ethiopia showing the inferred relative chronology and incorporating the dates and relative chronologies from Rapprich et al. (2016), Hutchison et al. (2016a), Fontijn et al. (2018) and Clarke et al. (2020). Units of uncertain correlation are shown with an approximation of their relative position. Symbols denote the samples in Fig. 14.

could pose a significant risk to the local population living within the caldera. The population within the caldera is estimated to be over 14,000 people based on the number of homes observed in satellite images (2836) and a rural occupancy rate of 5 (Ethiopian Public Health Institue (EPHI) and ICF, 2021); however, anecdotal evidence suggests the population is far greater than this estimate. Further work is required to fully delimit the risk posed by PDCs within the caldera (Clarke et al., 2020).

The Wendo Koshe Cone, as identified by Rapprich et al., (2016), is the youngest cone on the flanks of Urji and has previously been attributed as the source for the WKYP eruption. However, we find evidence which challenges this hypothesis. Throughout the central caldera, exposures of the Bedded Pumice unit (Section 3.3 & 3.4) show the classic architecture of a pumice cone eruption (SI A6). Close to the vent, beds are coarse-grained and chaotically bedded. At proximal locations, interbedded pumice fall and dilute to granular PDC deposits dominate, whilst distal deposits are massive pumice fall horizons (Clarke et al., 2020). The sequence in the central caldera consistently shows the Bedded Pumice horizon overlain by a paleosol and capped with a coarse-grained, obsidian bearing pumice (CC_B). This succession is so frequently observed we can confidently correlate it across multiple locations, including in exposures on the flanks of the Wendo Koshe Cone (Figs. 8 & 10). The occurrence of the Bedded Pumice unit on the flanks of the Wendo Koshe Cone, in conjunction with the fact it has the classic architecture of a pumice cone eruption, strongly suggests that the Bedded Pumice unit was emplaced during the formation of the Wendo Koshe Cone. The eruption followed the typical sequence of pumice cone forming eruptions as set out by Clarke et al. (2020), with an initial phase emplacing large blocks at proximal locations before establishing a highly unsteady plume that underwent periodic collapse, generating numerous dilute PDCs (SI A6). The deposition of massive pumice fall horizons at distal locations indicates the plume was established for a

period, but localised PDCs may have continued. The eruption may have concluded with the emplacement of a now buried lava, as is characteristic of pumice cone eruptions; however, this was not observed in the field or remote sensing imagery and is possibly buried by subsequent deposits.

One feature of the Wendo Koshe Cone is the absence of the WKYP on its flanks, despite deposits being seen at proximal locations (Fig. 10). The WKYP lacks the characteristics of a pumice cone eruption, and there is little evidence of the passage of PDCs indicating the plume was stable and sustained, depositing tephra over a large area (Fontijn et al., 2018; Rapprich et al., 2016). An outflow sheet on the northern flank of the Wendo Koshe Cone (Fig. 2F) has previously been attributed to the WKYP eruption (Rapprich et al., 2016) and appears to outcrop above the WKYP deposits. This raises two possible scenarios; (1) both the Bedded Pumice and the WKYP erupted from the same vent after a period of quiescence, (2) the Wendo Koshe Cone represents the remains of two cones, the first erupting the Bedded Pumice unit and the second forming in very close proximity first, erupting the WKYP and undergoing a flank collapse. Since pumice cones in the MER are thought to be monogenetic (Clarke et al., 2019, 2020) and we see evidence of vents in close proximity to one another (e.g., Eruption of CO4a from a vent near the Eastern Cone [Fig. 12]), we consider the second scenario to be the more likely. Whilst there is uncertainty surrounding this scenario, it does explain the nature of the observed deposits and highlights the discrete areas within the caldera where they have formed. It should be noted that further work is needed to fully understand the dynamics of pumice cone forming eruptions and whether they are in fact monogenetic.

Following the deposition of the WKYP, two other (smaller-scale) explosive eruptions occurred (CC_H & CG_E; Fig. 16); however, the origin of these eruptions have not been determined due to spatially inconsistent outcrops. They may be related to the more recent eruptions on Chabbi (CO5, CO5a, CO5b and CO6;[Fig. 11]) as they are only seen proximally to Chabbis edifice. Further work investigating the nature of these eruptions is required.

5.2.1. Biftu Tuff Cone

The Biftu Tuff Cone is one of the few vents not associated with the two main edifices, Urji and Chabbi. Its location outside the caldera wall (Fig. 2A & G) and away from the identified pre-existing faults makes it an apparently unique event at Corbetti. Investigation of the NW shore of Lake Hawassa revealed the presence of large, fully-dilute PDC deposits (see section 3.6), which are inferred to relate to the formation and collapse of the Biftu Tuff Cone. These deposits contain abundant reworked shells and display complex and varied sedimentary structures. Based on ^{14}C dating of *M. tuberculata* shells within an associated dilute PDC deposit on the Northwest shore of Lake Hawassa, the timing of the eruption can be broadly constrained to $<7375 \pm 54$ cal BP (Table 7). Previous studies have hypothesised a phreatomagmatic origin of the eruption resulting from the interaction with lake water during a relative high stand of Lake Hawassa (Clarke, 2020; Rapprich et al., 2016). The dates of these shells and stable isotope values are similar to those from other studies that demonstrate a high lake level and a wetter environment. In addition, studies on the nearby Ziway-Shalla basin have found evidence for multiple phases of shoreline retreat and advance during the late Pleistocene and early Holocene (Benvenuti et al., 2002; Gillespie et al., 1983; Olaka et al., 2010) reflecting changes in climate. Similarly, evidence from *M. tuberculata* shells from the Ziway-Shalla basin suggests higher precipitation levels in the rift during the early Holocene compared with today, which would contribute to rises in lake levels (Leng et al., 1999).

It is proposed that the eruption of the Biftu Tuff cone occurred at a time of high lake levels resulting in a phreatomagmatic eruption generating large quantities of ash and extensive, fully-dilute, PDCs. These PDCs likely travelled across the lake and subaqueously, incorporating lake sediment and shells as the flows travelled from the vent. Overlying the PDC at one locality (Site 12; Fig. 13) is a thin sequence of lake sediment capped with a shell bearing horizon. The ages of these shells are older than those in the underlying deposit. This 'upside down' age sequence likely occurred due to the reworking of old deposits which were emplaced during a period of high stand at Lake Hawassa. This supports observations of the continued fluctuations in the lake's water level during the early Holocene.

5.3. Recurrence rate and hazard implications

This field investigation identified 5–6 explosive and effusive eruptions at Corbetti over the last 2301 ± 120 cal BP (Fig. 16). Based on this, the recurrence rate over this period is approximately one eruption every 300–400 years, with four of these eruptions occurring on Chabbi. This evidence suggests volcanism is comparable with the approximated recurrence rate for Aluto (Fontijn et al., 2018; Hutchison et al., 2016b) and among the highest rates in the MER. These data, coupled with the active deformation occurring at the caldera, demonstrate the potential volcanic hazard Corbetti poses. A key question is understanding how any future volcanism will manifest itself at Corbetti. The contrasting styles of past volcanism across both Urji and Chabbi present two different hazards compared with the hazards posed by other MER volcanoes. Urji, like post-caldera vents at Aluto, shows a propensity to generate ash-rich PDCs which are likely to inundate densely populated areas within the caldera whilst the eruption of obsidian flows from Chabbi presents a more localised risk. This highlights the need for further hazard-based studies to fully constrain the ramifications of any future volcanism within the complex. This is especially important given the high population density and proposed development of a geothermal power plant within the caldera.

6. Conclusions

Here we have presented a detailed stratigraphy of activity at Corbetti over the course of its eruptive history, highlighting major explosive events and the range of volcanism experienced within the complex. Development of the edifice has been centred around eruptions from multiple vents emplacing large rhyolite lavas and pumice cones. We find previously undocumented evidence of lithic lag breccias and ignimbrites which may be associated with this eruption, recording the precursory and *syn*-phases of edifice collapse. The most recent activity at Corbetti centres around Urji and Chabbi, two low relief shields built up by eruptions from numerous vents. The styles of volcanism recorded at each edifice vary between the generation of multiple, highly localised PDCs and the eruption of obsidian lavas. *Re*-evaluation of the obsidian lavas on Chabbi has led to the identification of three additional units (CO4a, CO5a, CO5b), which were previously attributed to one of the larger deposits.

We propose that the most recent cone on Urji, the Wendo Koshe Cone, represents the remains of two cones, the first erupting the Bedded Pumice unit and the second erupting the WKYP. These are the two most well constrained post-caldera eruptions from Corbetti and are the most extensive deposits throughout the caldera. We find several locations on the post-caldera edifices that show vents opening close to older vents. We have constrained the age of the Biftu Tuff Cone eruption to $<7375 \pm 54$ cal BP through ^{14}C dating of shells incorporated into an associated PDC deposit. Carbon and oxygen isotope data from these shells also indicate the eruption likely occurred during a high-stand period at Lake Hawassa, raising the possibility of the lake water interacting with the eruption, resulting in the generation of the large-scale dilute PDCs observed.

Based on the new observations of eruptive deposits, we have determined a recurrence rate of between 300 and 400 years, highlighting that Corbetti has been one of the most active volcanoes within the MER during the Late Holocene. Corbetti is also seen to have a propensity to generate dilute, highly localised PDCs. The frequency with which these deposits are seen within the caldera highlights that PDCs are a

significant hazard for future eruptions. Therefore, we recommend further investigating the PDC-related hazards, especially considering plans to develop a geothermal powerplant within the caldera.

Authors statement

David J Colby: Conceptualization, Investigation, Writing - Original Draft, Project administration,Visualization.

David M Pyle: Conceptualization, Writing - Review & Editing, Supervision, Project administration.

Karen Fontijn: Conceptualization, Writing - Review & Editing, Supervision, Resources, Project administration

Tamsin A Mather: Conceptualization, Writing - Review & Editing, Supervision, Project administration, Funding acquisition.

Abate A Melaku: Writing - Review & Editing, Project administration.

Million A Megesha: Writing - Review & Editing, Project administration.

Gezahegn Yirgu: Conceptualization, Writing - Review & Editing, Project administration.

Declaration of Competing Interest

The authors declare that they have no known competing financial interests or personal relationships that could have appeared to influence the work reported in this paper.

Acknowledgements

This work was supported by the Natural Environment Research Council via grant NE/L013932/1 (RiftVolc) and an Oxford DTP studentship (NE/L002612/1) to D.C. We would like to thank Seid Abubaker of Ethioder and guide Hamiyou Bekera for their support in the field and for ensuring a safe and productive field trip. Fieldwork and sample export was kindly permitted by the authroities of the Oromia region and Ministry of Mines and Petroleum of Ethiopia, respectively. We would also like to thank Owen Green for his help with sample preparation and Activation Laboratories and Beta Analytic for conducting the geochemical analysis and carbon dating respectively. We thank Vladislav Rapprich and Stéphane Scaillet for their reviews which have helped to improve this paper.

Appendix A. Supplementary data

Supplementary data to this article can be found online at https://doi.org/10.1016/j.jvolgeores.2022.107580.

References

Agostini, A., Bonini, M., Corti, G., Sani, F., Mazzarini, F., 2011. Fault architecture in the Main Ethiopian Rift and comparison with experimental models: implications for rift evolution and Nubia-Somalia kinematics. Earth Planet. Sci. Lett. 301, 479–492. https://doi.org/10.1016/j.epsl.2010.11.024.

Altaye, E., 1984. Geology and Surface Alteration of the Corbetti Caldera. Auckland.

Aspinall, W.P., Auker, M., Hincks, T., Mahony, S., Nadim, F., Pooley, J., Sparks, S., Syre, E., 2011. Volcano Hazard and Exposure in GFDRR Priority Countries and Risk Mitigation Measures-GFDRR, Volcano Risk Study. Bristol University Cabot Institute and NGI Norway for the World Bank: NGI Report 20100806, Bristol. Oslo.

Benvenuti, M., Carnicelli, S., Belluomini, G., Dainelli, N., Di Grazia, S., Ferrari, G.A., Iasio, C., Sagri, M., Ventra, D., Atnafu, B., Kebede, S., 2002. The Ziway-Shala lake basin (main Ethiopian rift, Ethiopia): a revision of basin evolution with special reference to the late Quaternary. J. Afr. Earth Sci. 35, 247–269. https://doi.org/10.1016/S0899-5362(02)00036-2.

Biggs, J., Bastow, I.D., Keir, D., Lewi, E., 2011. Pulses of deformation reveal frequently recurring shallow magmatic activity beneath the Main Ethiopian Rift. Geochem. Geophys. Geosyst. 12, 1–11. https://doi.org/10.1029/2011GC003662.

Boone, S.C., Kohn, B.P., Gleadow, A.J.W., Morley, C.K., Seiler, C., Foster, D.A., 2019. Birth of the East African Rift System: nucleation of magmatism and strain in the Turkana Depression. Geology 47, 886–890. https://doi.org/10.1130/g46468.1.

Branney, M.J., Kokelaar, P., 2002. Pyroclastic Density Currents and the Sedimentation of Ignimbrites. In: Geological Society, London, Memoirs. Geological Society of London. https://doi.org/10.1144/GSL.MEM.2003.027.

Brown, R.J., Branney, M.J., Maher, C., Davila-Harris, P., 2010. Origin of accretionary lapilli within ground-hugging density currents: evidence from pyroclastic couplets on Tenerife. Geol. Soc. Am. Bull. 122, 305–320. https://doi.org/10.1130/B26449.1.

Brown, R.J., Bonadonna, C., Durant, A.J., 2012. A review of volcanic ash aggregation. Phys. Chem. Earth 45–46, 65–78. https://doi.org/10.1016/j.pce.2011.11.001.

Casey, M., Ebinger, C.J., Keir, D., Gloaguen, R., Mohamed, F., 2006. Strain accommodation in transitional rifts: extension by magma intrusion and faulting in Ethiopian rift magmatic segments. Geol. Soc. Spec. Publ. 259, 143–163. https://doi.org/10.1144/GSL.SP.2006.259.01.13.

Clarke, B.A., 2020. Post-Caldera Eruptions and Pyroclastic Density Current Hazard in the Main Ethiopian Rift. The University of Edinburgh.

Clarke, B., Calder, E.S., Dessalegn, F., Fontijn, K., Cortés, J.A., Naylor, M., Butler, I., Hutchison, W., Yirgu, G., 2019. Fluidal pyroclasts reveal the intensity of peralkaline rhyolite pumice cone eruptions. Nat. Commun. 10, 2010. https://doi.org/10.1038/s41467-019-09947-8.

Clarke, B., Tierz, P., Calder, E., Yirgu, G., 2020. Probabilistic volcanic hazard assessment for pyroclastic density currents from pumice cone eruptions at Aluto Volcano, Ethiopia. Front. Earth Sci. 8, 1–19. https://doi.org/10.3389/feart.2020.00348.

Corti, G., 2009. Continental rift evolution: from rift initiation to incipient break-up in the Main Ethiopian Rift, East Africa. Earth Sci. Rev. 96, 1–53. https://doi.org/10.1016/j.earscirev.2009.06.005.

Corti, G., Maestrelli, D., Sani, F., 2022. Large-to local-scale control of pre-existing structures on continental rifting: examples from the Main Ethiopian Rift, East Africa. Front. Earth Sci. 10, 1–18. https://doi.org/10.3389/feart.2022.808503.

Costa, F., Shea, T., Ubide, T., 2020. Diffusion chronometry and the timescales of magmatic processes. Nat. Rev. Earth Environ. 1, 201–214. https://doi.org/10.1038/s43017-020-0038-x.

Di Paola, G.M., 1971. Geology of the Corbetti Caldera area (Main Ethiopian Rift Valley). Bull. Volcanol. 35, 497–506. https://doi.org/10.1007/BF02596970.

Druitt, T.H., 1985. Vent evolution and lag breccia formation during the Cape Riva Eruption of Santorini, Greece. J. Geol. 93, 439–454. https://doi.org/10.1086/628965.

Duffield, W.A., Bacon, C.R., Roquemore, G.R., 1979. Origin of reverse-graded beddeing in air-fall pumice, Coso Range, California. J. Volcanol. Geotherm. Res. 5, 35–48.

Ebinger, C., 2005. Continental break-up: the East African perspective. Astron. Geophys. 46, 2.16-2.21. https://doi.org/10.1111/j.1468-4004.2005.46216.x.

Ebinger, C.J., Casey, M., 2001. Continental breakup in magmatic provinces: an Ethiopian example. Geology 29, 527–530. https://doi.org/10.1130/0091-7613(2001)029<0527:CBIMPA>2.0.CO;2.

Ethiopian Public Health Institue (EPHI), ICF, 2021. Ethiopia Mini Demographic and Health Survey 2019: Final Report. Rockville, Maryland, USA.

Fontijn, K., McNamara, K., Zafu Tadesse, A., Pyle, D.M., Dessalegn, F., Hutchison, W., Mather, T.A., Yirgu, G., 2018. Contrasting styles of post-caldera volcanism along the Main Ethiopian Rift: Implications for contemporary volcanic hazards. J. Volcanol. Geotherm. Res. 356, 90–113. https://doi.org/10.1016/j.jvolgeores.2018.02.001.

Gillespie, R., Street-perrott, F.A., Switsur, R., 1983. Post-glacial arid episodes in Ethiopia have implications for climate prediction. Nature 306, 680–683. https://doi.org/10.1038/306680a0.

Gíslason, G., Eysteinsson, H., Björnsson, G., Harðardóttir, V., 2015. Results of surface exploration in the Corbetti Geothermal Area, Ethiopia. World Geotherm. Congr. 2015, 1–10.

Gleeson, M.L.M., Stock, M.J., Pyle, D.M., Mather, T.A., Hutchison, W., Yirgu, G., Wade, J., 2017. Constraining magma storage conditions at a restless volcano in the Main Ethiopian Rift using phase equilibria models. J. Volcanol. Geotherm. Res. 337, 44–61. https://doi.org/10.1016/j.jvolgeores.2017.02.026.

Gottsmann, J., Biggs, J., Lloyd, R., Biranhu, Y., Lewi, E., 2020. Ductility and compressibility accommodate high magma flux beneath a silicic continental rift Caldera: insights from Corbetti Caldera (Ethiopia). Geochem. Geophys. Geosyst. 21 https://doi.org/10.1029/2020gc008952.

Grosse, P., Kervyn, M., 2018. Morphometry of terrestrial shield volcanoes. Geomorphology 304, 1–14. https://doi.org/10.1016/j.geomorph.2017.12.017.

Hunt, J.A., Pyle, D.M., Mather, T.A., 2019. The geomorphology, structure, and lava flow dynamics of peralkaline rift volcanoes from high-resolution digital elevation models. Geochem. Geophys. Geosyst. https://doi.org/10.1029/2018GC008085.

Hutchison, W., Mather, T.A., Pyle, D.M., Biggs, J., Yirgu, G., 2015. Structural controls on fluid pathways in an active rift system: a case study of the Aluto volcanic complex. Geosphere 11, 542–562. https://doi.org/10.1130/GES01119.1.

Hutchison, W., Fusillo, R., Pyle, D.M., Mather, T.A., Blundy, J.D., Biggs, J., Yirgu, G., Cohen, B.E., Brooker, R.A., Barfod, D.N., Calvert, A.T., 2016a. A pulse of mid-Pleistocene rift volcanism in Ethiopia at the dawn of modern humans. Nat. Commun. 7, 1–12. https://doi.org/10.1038/ncomms13192.

Hutchison, W., Pyle, D.M., Mather, T.A., Yirgu, G., Biggs, J., Cohen, B.E., Barfod, D.N., Lewi, E., 2016b. The eruptive history and magmatic evolution of Aluto volcano: new insights into silicic peralkaline volcanism in the Ethiopian rift. J. Volcanol. Geotherm. Res. 328, 9–33. https://doi.org/10.1016/j.jvolgeores.2016.09.010.

Iddon, F., Edmonds, M., 2020. Volatile-rich magmas distributed through the upper crust in the Main Ethiopian Rift. Geochem. Geophys. Geosyst. 21 https://doi.org/10.1029/2019GC008904.

Iddon, F., Jackson, C., Hutchison, W., Fontijn, K., Pyle, D.M., Mather, T.A., Yirgu, G., Edmonds, M., 2019. Mixing and crystal scavenging in the main Ethiopian rift revealed by trace element systematics in feldspars and glasses. Geochem. Geophys. Geosyst. 20, 230–259. https://doi.org/10.1029/2018GC007836.

Jackson, M.D., Blundy, J., Sparks, R.S.J., 2018. Chemical differentiation, cold storage and remobilization of magma in the Earth's crust. Nature 564, 405–409. https://doi.org/10.1038/s41586-018-0746-2.

Jordan, N.J., Rotolo, S.G., Williams, R., Speranza, F., McIntosh, W.C., Branney, M.J., Scaillet, S., 2018. Explosive eruptive history of Pantelleria, Italy: Repeated caldera collapse and ignimbrite emplacement at a peralkaline volcano. J. Volcanol. Geotherm. Res. 349, 47–73. https://doi.org/10.1016/j.jvolgeores.2017.09.013.

Kendall, J.M., Stuart, G.W., Ebinger, C.J., Bastow, I.D., Keir, D., 2005. Magma-assisted rifting in Ethiopia. Nature 433, 146–148. https://doi.org/10.1038/nature03161.

Kurz, T., Gloaguen, R., Ebinger, C., Casey, M., Abebe, B., 2007. Deformation distribution and type in the Main Ethiopian Rift (MER): a remote sensing study. J. Afr. Earth Sci. 48, 100–114. https://doi.org/10.1016/j.jafrearsci.2006.10.008.

Lamb, A.L., Leng, M.J., Lamb, H.F., Telford, R.J., Mohammed, M.U., 2002. Climatic and non-climatic effects on the δ18O and δ13C compositions of Lake Awassa, Ethiopia, during the last 6.5 ka. Quat. Sci. Rev. 21, 2199–2211. https://doi.org/10.1016/S0277-3791(02)00087-2.

Lavayssière, A., Greenfield, T., Keir, D., Ayele, A., Kendall, J.-M., 2019. Local seismicity near the actively deforming Corbetti volcano in the Main Ethiopian Rift. J. Volcanol. Geotherm. Res. https://doi.org/10.1016/j.jvolgeores.2019.06.008.

Leng, M.J., Lamb, A.L., Lamb, H.F., Telford, R.J., 1999. Palaeoclimatic implications of isotopic data from modern and early Holocene shells of the freshwater snail Melanoides tuberculata, from lakes in the Ethiopian Rift Valley. J. Paleolimnol. 21, 97–106. https://doi.org/10.1023/A:1008079219280.

Lloyd, R., Biggs, J., Birhanu, Y., Wilks, M., Gottsmann, J., Kendall, J.M., Ayele, A., Lewi, E., Eysteinsson, H., 2018a. Sustained Uplift at a Continental Rift Caldera. J. Geophys. Res. Solid Earth 123, 5209–5226. https://doi.org/10.1029/2018JB015711.

Lloyd, R., Biggs, J., Wilks, M., Nowacki, A., Kendall, J.M., Ayele, A., Lewi, E., Eysteinsson, H., 2018b. Evidence for cross rift structural controls on deformation and seismicity at a continental rift caldera. Earth Planet. Sci. Lett. 487, 190–200. https://doi.org/10.1016/j.epsl.2018.01.037.

Loughlin, S.C., Sparks, R.S.J., Brown, S.K., Jenkins, S.F., Vye-Brown, C. (Eds.), 2015. Global Volcanic Hazards and Risk, Metrologia. Cambridge University Press, Cambridge, UK.

MacDonald, R., 1974. Nomenclature and petrochemistry of the peralkaline oversaturated extrusive rocks. Bull. Volcanol. 38, 498–516. https://doi.org/10.1007/BF02596896.

Macdonald, R., Gibson, I.L., 1969. Pantelleritic obsidians from the volcano Chabbi (Ethiopia). Contrib. Mineral. Petrol. 24, 239–244. https://doi.org/10.1007/BF00376050.

Macdonald, R., Bagiński, B., Ronga, F., Dzierzanowski, P., Lustrino, M., Marzoli, A., Melluso, L., 2012. Evidence for extreme fractionation of peralkaline silicic magmas, the Boseti volcanic complex, Main Ethiopian Rift. Mineral. Petrol. 104, 163–175. https://doi.org/10.1007/s00710-011-0184-4.

Maestrelli, D., Corti, G., Bonini, M., Montanari, D., Sani, F., 2022. Caldera collapse and tectonics along the Main Ethiopian Rift: reviewing possible relationships. Compt. Rend. Géosci. 353, 91–109. https://doi.org/10.5802/crgeos.63.

Mahood, G.A., 1984. Pyroclastic rocks and calderas associated with strongly peralkaline magmatism. J. Geophys. Res. 89, 8540. https://doi.org/10.1029/JB089iB10p08540.

Martin-Jones, C.M., Lane, C.S., Pearce, N.J.G., Smith, V.C., Lamb, H.F., Schaebitz, F., Viehberg, F., Brown, M.C., Frank, U., Asrat, A., 2017. Recurrent explosive eruptions from a high-risk Main Ethiopian Rift volcano throughout the Holocene. Geology 45, 1127–1130. https://doi.org/10.1130/G39594.1.

Mazzarini, F., Corti, G., Manetti, P., Innocenti, F., 2004. Strain rate and bimodal volcanism in the continental rift: Debre Zeyt volcanic field, northern MER, Ethiopia. J. Afr. Earth Sci. 39, 415–420. https://doi.org/10.1016/j.jafrearsci.2004.07.025.

McNamara, K., Cashman, K.V., Rust, A.C., Fontijn, K., Chalié, F., Tomlinson, E.L., Yirgu, G., 2018. Using lake sediment Cores to improve records of volcanism at aluto volcano in the Main Ethiopian Rift. Geochem. Geophys. Geosyst. 19, 3164–3188. https://doi.org/10.1029/2018GC007686.

Mohr, P.A., 1966. Chabbi Volcano (Ethiopia). Bull. Volcanol. 797–815.

Mohr, P., Mitchell, J.G., Raynolds, R.G.H., 1980. Quaternary volcanism and faulting at O'A caldera, central ethiopian rift. Bull. Volcanol. 43, 173–189. https://doi.org/10.1007/BF02597619.

Olaka, L.A., Odada, E.O., Trauth, M.H., Olago, D.O., 2010. The sensitivity of East African rift lakes to climate fluctuations. J. Paleolimnol. 44, 629–644. https://doi.org/10.1007/s10933-010-9442-4.

Peccerillo, A., Donati, C., Santo, A.P., Orlando, A., Yirgu, G., Ayalew, D., 2007. Petrogenesis of silicic peralkaline rocks in the Ethiopian rift: Geochemical evidence and volcanological implications. J. Afr. Earth Sci. 48, 161–173. https://doi.org/10.1016/j.jafrearsci.2006.06.010.

Pizzi, A., Coltorti, M., Abebe, B., Disperati, L., Sacchi, G., Salvini, R., 2006. The Wonji fault belt (Main Ethiopian Rift): structural and geomorphological constrains and GPS monitoring. In: Yirgu, G., Ebinger, C.J., Maguire, P.K.H. (Eds.), The Afar Volcanic Province within the East African Rift System. Geological Society of London, pp. 191–207. Special Publications.

Purcell, P.G., 2018. Re-imagining and re-imaging the development of the East African Rift. Pet. Geosci. 24, 21–40. https://doi.org/10.1144/petgeo2017-036.

Rampey, M.L., Oppenheimer, C., Pyle, D.M., Yirgu, G., 2010. Caldera-forming eruptions of the Quaternary Kone Volcanic complex, Ethiopia. J. Afr. Earth Sci. 58, 51–66. https://doi.org/10.1016/j.jafrearsci.2010.01.008.

Rapprich, V., Žáček, V., Verner, K., Erban, V., Goslar, T., Bekele, Y., Legesa, F., Hroch, T., Hejtmánková, P., 2016. Wendo Koshe Pumice: the latest Holocene silicic explosive eruption product of the Corbetti Volcanic System (Southern Ethiopia). J. Volcanol. Geotherm. Res. 310, 159–171. https://doi.org/10.1016/j.jvolgeores.2015.12.008.

Reimer, P.J., Austin, W.E.N., Bard, E., Bayliss, A., Blackwell, P.G., Bronk Ramsey, C., Butzin, M., Cheng, H., Edwards, R.L., Friedrich, M., Grootes, P.M., Guilderson, T.P., Hajdas, I., Heaton, T.J., Hogg, A.G., Hughen, K.A., Kromer, B., Manning, S.W., Muscheler, R., Palmer, J.G., Pearson, C., Van Der Plicht, J., Reimer, R.W., Richards, D.A., Scott, E.M., Southon, J.R., Turney, C.S.M., Wacker, L., Adolphi, F., Büntgen, U., Capano, M., Fahrni, S.M., Fogtmann-Schulz, A., Friedrich, R., Köhler, P., Kudsk, S., Miyake, F., Olsen, J., Reinig, F., Sakamoto, M., Sookdeo, A., Talamo, S., 2020. The IntCal20 northern hemisphere radiocarbon age calibration curve (0-55 cal kBP). Radiocarbon 62, 725–757. https://doi.org/10.1017/RDC.2020.41.

Robertson, E.A.M., Biggs, J., Cashman, K.V., Floyd, M.A., Vye-Brown, C., 2016. Influence of regional tectonics and pre-existing structures on the formation of elliptical calderas in the Kenyan Rift. Geol. Soc. Spec. Publ. 420, 43–67. https://doi.org/10.1144/SP420.12.

Ronga, F., Lustrino, M., Marzoli, A., Melluso, L., 2009. Petrogenesis of a basalt-comendite-pantellerite rock suite: the Boseti Volcanic complex (Main Ethiopian Rift). Mineral. Petrol. 98, 227–243. https://doi.org/10.1007/s00710-009-0064-3.

Rooney, T.O., Hart, W.K., Hall, C.M., Ayalew, D., Ghiorso, M.S., Hidalgo, P., Yirgu, G., 2012. Peralkaline magma evolution and the tephra record in the Ethiopian Rift. Contrib. Mineral. Petrol. 164, 407–426. https://doi.org/10.1007/s00410-012-0744-6.

Shand, S.J., 1927. On the relations between silica, alumina, and the bases in Eruptive Rocks, considered as a means of classification. Geol. Mag. 64, 446–449. https://doi.org/10.1017/S0016756800103760.

Simmons, J.M., Cas, R.A.F., Druitt, T.H., Folkes, C.B., 2016. Complex variations during a caldera-forming Plinian eruption, including precursor deposits, thick pumice fallout, co-ignimbrite breccias and climactic lag breccias: the 184 ka lower Pumice 1 eruption sequence, Santorini, Greece. J. Volcanol. Geotherm. Res. 324, 200–219. https://doi.org/10.1016/j.jvolgeores.2016.05.013.

Tadesse, A.Z., Ayalew, D., Pik, R., Yirgu, G., Fontijn, K., 2019. Magmatic evolution of the Boku Volcanic complex, Main Ethiopian Rift. J. Afr. Earth Sci. 149, 109–130. https://doi.org/10.1016/j.jafrearsci.2018.08.003.

Tadesse, A.Z., Fontijn, K., Melaku, A.A., Gebru, E.F., Smith, V.C., Tomlinson, E., Barfod, D., Gopon, P., Bégué, F., Caricchi, L., Laha, P., Terryn, H., Gudbrandsson, S., Yirgu, G., Ayalew, D., 2022. Eruption frequency and magnitude in a geothermally active continental rift: the Bora-Baricha-Tullu Moye volcanic complex, Main Ethiopian Rift. J. Volcanol. Geotherm. Res. 107471 https://doi.org/10.1016/j.jvolgeores.2022.107471.

Vidal, C.M., Lane, C.S., Asrat, A., Barfod, D.N., Mark, D.F., Tomlinson, E.L., Tadesse, A.Z., Yirgu, G., Deino, A., Hutchison, W., Mounier, A., Oppenheimer, C., 2022. Age of the oldest known Homo sapiens from eastern Africa. Nature. https://doi.org/10.1038/s41586-021-04275-8.

Vye-Brown, C., Sparks, R.S.J., Lewi, E., Mewa, G., Asrat, A., Loughlin, S.C., Mee, K., Wright, T.J., 2015. Ethiopian Volcanic Hazards: A Changing Research Landscape.

Webb, P.K., Weaver, S.D., 1975. Trachyte shield volcanoes: a new volcanic form from South Turkana, Kenya. Bull. Volcanol. 39 (2), 294–312. https://doi.org/10.1007/BF02597833.

White, J.C., Parker, D.F., Ren, M., 2009. The origin of trachyte and pantellerite from Pantelleria, Italy: insights from major element, trace element, and thermodynamic modelling. J. Volcanol. Geotherm. Res. 179, 33–55. https://doi.org/10.1016/j.jvolgeores.2008.10.007.

WoldeGariel, G., Walter, R.C., Aronson, J.L., Hart, W.K., 1992. Geochronology and distribution of silicic volcanic rocks of Plio-Pleistocene age from the Central Sector of the Main Ethiopian Rift. Quat. Int. 13, 69–76.